The Impacts of California's San Francisco Bay Area Gap on Precipitation Observed in the Sierra Nevada during HMT and CalWater

ALLEN B. WHITE AND PAUL J. NEIMAN

NOAA/Earth System Research Laboratory/Physical Sciences Division, Boulder, Colorado

JESSIE M. CREAMEAN AND TIMOTHY COLEMAN

Cooperative Institute for Research in Environmental Sciences, University of Colorado Boulder, and NOAA/Earth System Research Laboratory/Physical Sciences Division, Boulder, Colorado

F. MARTIN RALPH

Scripps Institution of Oceanography, University of California, San Diego, La Jolla, California

KIMBERLY A. PRATHER

University of California, San Diego, La Jolla, California

(Manuscript received 27 August 2014, in final form 15 December 2014)

ABSTRACT

Atmospheric rivers (ARs) are narrow regions of enhanced water vapor transport, usually found on the warm-sector side of the polar cold front in many midlatitude storms formed primarily over the oceans. Nonbrightband (NBB) rain is a shallow orographic rainfall process driven by collision and coalescence that has been observed in some of these storms. NBB rain accounts for about one-third, on average, of the total winter season rainfall occurring at a coastal mountain site in Northern California. During the California Energy Commission's CalWater project, nearly the same fraction of NBB rain was observed at a northern Sierra Nevada foothills site as compared to the coastal mountains, whereas less than half of the fractional amount of NBB rain was observed at a southern Sierra Nevada foothills site. Both Sierra Nevada sites often experience terrain-induced blocked flow, that is, Sierra barrier jet (SBJ) during landfalling winter storms. However, the northern Sierra Nevada site often is oriented geographically downwind of a gap in the coastal terrain near San Francisco during AR landfall. This gap allows maritime air in the AR to arrive at the northern site and enhance the collision–coalescence process in orographic feeder clouds as compared with the southern site. As a result, a greater amount and intensity of NBB rain and overall precipitation was produced at the northern site. This study uses a variety of observations collected in the coastal and Sierra Nevada ranges from the Hydrometeorology Testbed and CalWater field campaigns to document this behavior. A detailed case study provides additional context on the interaction between AR flow, the SBJ, and precipitation processes.

1. Introduction

Some of the recent research conducted under the National Oceanic and Atmospheric Administration (NOAA)'s Hydrometeorology Testbed (HMT; Ralph et al. 2005, 2013a) has focused on a shallow rainfall process driven by collision and coalescence. This shallow rainfall is often undetected by the National Weather Service (NWS)'s operational scanning radar network, but it can produce rain rates that are capable of creating floods (e.g., White et al. 2003; Matrosov et al. 2014). This is especially true in California, where flooding from wintertime precipitation is often a concern. Originally, it was believed that this shallow rainfall process would occur more prevalently over the coastal mountain ranges than over the Sierra Nevada in California, since the higher mountains of the Sierra Nevada would force deeper atmospheric ascent and produce deeper precipitating cloud systems that would extend

---

Corresponding author address: Dr. Allen B. White, NOAA/Earth System Research Laboratory, R/PS2, 325 Broadway, Boulder, CO 80305.
E-mail: allen.b.white@noaa.gov

DOI: 10.1175/JHM-D-14-0160.1

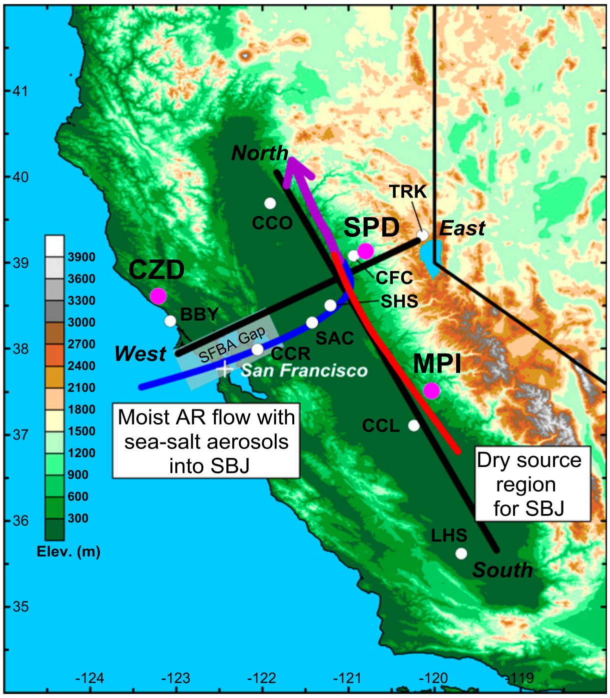

FIG. 1. Terrain base map of California, with a schematic showing the interaction (purple curve) between unimpeded AR flow through the SFBA gap (blue curve) with the SBJ flowing northward along the east side of the Central Valley (red curve) during a typical winter storm with an imbedded AR. Instrumented sites (listed in Table 3) with Doppler wind profilers (white dots) and cross sections (black lines) used to represent AR and SBJ flow characteristics (see Fig. 9). The S-PROF observing sites at CZD, MPI, and SPD are indicated by pink dots.

well above the melting level. This notion was disproved when it was recently discovered that a site in the northern Sierra Nevada located near Sugar Pine Dam (SPD; Fig. 1) had as large of a contribution to seasonal rainfall from this shallow rainfall process, on average, as did a climatologically wet site in the coastal range of Sonoma County near Cazadero (CZD; Fig. 1), north of San Francisco (Neiman et al. 2005). Herein, this paper examines this apparent paradox using observations collected during a series of field experiments called the California Energy Commission's CalWater project. In particular, we use measurements from the CalWater Early Start (Ault et al. 2011) and CalWater (Creamean et al. 2013) field campaigns. Additional observations were supported by HMT.

The primary observing system used to document the vertical structure of precipitation in previous studies on this subject, as well as the current study, is NOAA's S-band precipitation profiler (S-PROF; White et al. 2000; see section 3 for more details). Four previous HMT studies summarized here, among possibly others, have contributed to improving our collective understanding of this shallow rainfall process observed on the U.S. West Coast.

White et al. (2003) established the technique of using vertical profiles of radar reflectivity and Doppler vertical velocity (DVV) collected with an S-PROF to examine the microphysical properties of rainfall observed in the coastal mountains of Northern California. In particular, they developed an automated rainfall process partitioning algorithm that used S-PROF data to distinguish between brightband rain (BB rain), that is, precipitation caused by ice falling through a melting layer to produce a radar bright band (White et al. 2002) and eventually rainfall at the surface, and nonbrightband rain (NBB rain), that is, a much shallower rainfall process that does not exhibit a melting layer bright band. Their results indicated that NBB rain contributed about one-third of the total rainfall measured at CZD during the 1997/98 California Land-Falling Jets Experiment (CALJET) field season. Matrosov et al. (2014) later found a similar NBB rain contribution (34%) at CZD averaged over six winter wet seasons. In addition, White et al. (2003) showed statistically that NBB rain had vastly different profiles of radar reflectivity and DVV as compared to BB rain. They concluded that NBB rain consists of a drop size distribution weighted much more heavily to smaller drops. Furthermore, without ice processes contributing substantially, NBB rain should be formed primarily by collision and coalescence in a relatively warm, moist cloud environment.

Neiman et al. (2005) extended the rainfall process partitioning analysis to S-PROF data collected at four observing sites in California and Oregon and over four winter seasons. These results confirmed the shallow nature of NBB compared to BB rain. Neiman et al. (2005) also examined the synoptic-scale conditions that led to the formation of BB and NBB rain at CZD using both composite NCEP–NCAR reanalyses products and Geostationary Operational Environmental Satellite (GOES) cloud-top temperature data. The BB rain composites exhibited stronger and deeper ascent over CZD than for the typically shallower NBB rain, consistent with the GOES composites that showed, on average, 20-K warmer (2.3-km shallower) cloud tops for NBB rain. Composite soundings for both rain types possessed low-level potential instability, but the sounding for NBB rain was warmer and moister with stronger low-level upslope flow, thus implying that orographically forced rainfall is enhanced during NBB rain conditions.

Kingsmill et al. (2006) used a synoptic classification scheme to determine when NBB was most likely to occur. They identified five distinct synoptic regimes (cold sector, warm front, warm sector, cold front, and cool sector) based on a simplified conceptual model. NBB rain occurred most often during the warm-frontal, warm-sector, and cool-sector regimes. Kingsmill et al. (2006) also analyzed the profile of radar reflectivity below the freezing level and found that NBB rain commonly had a positive reflectivity slope (reflectivity increasing with decreasing altitude), supporting the hypothesis that NBB rain is driven primarily by collision and coalescence at low altitudes. They found that even when BB rain was present over CZD, the relationship between low-level radar reflectivity and rain rate indicated a larger number of small drops than expected by a Marshall–Palmer drop size distribution, demonstrating that low-level warm rain processes were occurring even during BB rain conditions. White et al. (2003) referred to this combination of processes working together as ''hybrid'' rain.

Martner et al. (2008) further explored the microphysical differences between BB and NBB rain using drop size distribution measurements collected with Joss–Waldvogel impact disdrometers. Their results indicated that although the liquid water contents for hundreds of different 10-min samples of the drop size distributions for each rainfall type were nearly identical, significant differences occurred in other derived statistics, most notably reflectivity, mean-volume diameter, total number of drops, and slope of the drop size spectrum. Martner et al. (2008) also used the S-PROF observations to estimate the depth of the rain clouds by locating the highest altitude where a detectable signal was measured in each radar profile (i.e., the echo top). They concluded that high, cold echo-top clouds almost always produced larger hydrometeors and a bright band, but low, warm echo-top clouds almost always failed to generate large drops and a bright band (even when the echo top was below freezing).

In this paper, we expand on these previous studies by

1) extending the record of annual rainfall process partitioning statistics for the California coast and for two new sites in the Sierra Nevada;
2) reconciling why a northern Sierra Nevada site behaves similarly to a coastal mountain site in terms of these rainfall process partitioning statistics; and
3) providing an in-depth case study analysis to demonstrate how meteorological forcing controls orographic precipitation intensity, including the fractional contribution of rain produced by the shallow NBB rain process.

We begin with a description of CalWater that encompasses the case study period presented in section 5.

2. CalWater

The primary goals of CalWater were to study how aerosols impact precipitation in the Sierra Nevada (Ault et al. 2011; Creamean et al. 2013, 2015) and how atmospheric rivers (ARs) create heavy orographic precipitation that can lead to flooding (Ralph et al. 2004, 2006, 2013b; Neiman et al. 2008; Guan et al. 2010; Lavers et al. 2011; Moore et al. 2012). This current study is at the intersection of the primary CalWater subject areas as it attempts to answer two related questions. First, does the inland penetration of moist maritime air in ARs lead to forming more NBB rain over the portion of the Sierra Nevada that is most often downwind from the San Francisco Bay Area (SFBA) gap (shown in Fig. 1) as compared to the portion of the Sierra Nevada that is more likely to experience AR conditions that have been influenced by upstream terrain? Second, can we verify that maritime air with sea salt aerosols is making its way to the Sierra Nevada site where more NBB rain is observed? These hypothetical questions are illustrated schematically in Fig. 1.

The CalWater Early Start project (January–March 2009) brought together ground-based aerosol and hydrometeorological sensors, including an S-PROF, at SPD in the Sierra Nevada. During the two weeks of aerosol sampling at the end of February and beginning of March, 250–500 mm of rain or liquid equivalent snow was fortuitously observed. The precipitation came mostly during two meteorologically similar AR events, one of which showed the presence of Asian dust as the primary aerosol content within the precipitation (Ault et al. 2011).

For the first winter season of the primary CalWater field study (January–March 2010), NOAA and the University of California, San Diego, added another combined aerosol–hydrometeorology field site in the southern Sierra Nevada at Mariposa (MPI) that included another S-PROF, and a newly sited Doppler wind profiler (see section 5a) at Concord, California, to document the western edge of the Sierra barrier jet (SBJ), and enhancements to other HMT field sites. Several major storms were documented, including some with well-defined AR, aerosol, and SBJ conditions (Creamean et al. 2015).

The final CalWater field study (from December 2010 to March 2011) included several flights on the U.S. Department of Energy's Gulfstream-1 (G-1) research aircraft to document cloud microphysics and aerosol conditions aloft, in coordination with ground-based observations in the Sierra Nevada and Central Valley (Creamean et al. 2013). The S-PROFs were again deployed to SPD and MPI. Also, a high-powered scanning C-band Doppler radar plus a balloon sounding system from NOAA were deployed in the Central Valley (north of Sacramento) to monitor the Sierra barrier jet and possible interactions with landfalling ARs (Kingsmill et al. 2013). Together, the CalWater Early Start and two subsequent CalWater field studies comprise what is now referred to as CalWater 1 (2009–11). A second proposed 5-yr phase of experiments, called CalWater 2, began in 2014.

This paper also takes advantage of observations available throughout California that are part of an HMT-Legacy observing system described by White et al. (2013). For example, we use the GPS-derived integrated water vapor (IWV) measurements available from this HMT-Legacy observing system to compare and contrast the inland penetration of IWV associated with an AR at northern and southern Sierra Nevada observing sites for the case study presented in section 5.

3. Rainfall process partitioning algorithm statistics

The S-PROF was designed specifically with a large dynamic range to capture the full range of rainfall intensities associated with winter storms observed along the U.S. West Coast without saturating the radar's receiver. This goal was accomplished by running the radar sequentially in three different operating modes with different sensitivities, all either with 45-, 60-, or 100-m vertical resolution, depending on the field experiment. The total dynamic range resulting from this sampling strategy was initially 96 dB. Later digital receivers were employed in the S-PROF design, which added another ~20 dB of dynamic range. During postexperiment analysis, the modes are intercalibrated and combined to produce a single-mode profile of uncalibrated equivalent radar reflectivity factor (dBZ_e) and a corresponding profile of DVV (m s^{-1}). When available, surface reflectivity measurements from a collocated disdrometer are used to provide a radar calibration for the combined-mode radar reflectivity. However, the rainfall process partitioning algorithm described below does not depend on an absolute radar calibration. Although this algorithm has not undergone substantial changes since it was originally described by White et al. (2003), more than a decade has elapsed since that publication. Therefore, we provide a brief description of the algorithm.

Precipitation data from a gauge collocated with the S-PROF are analyzed every 30 min. If there is >0.5 mm of accumulation over 30 min, then the algorithm is applied to the S-PROF data collected during that period. Each S-PROF profile of radar reflectivity and DVV is examined to determine if precipitation is present in the profile using specified threshold criteria. This step is necessary partly because the radar samples have greater temporal resolution (typically 1 min or less for a combined-mode profile) than the rain gauge (2 min). If precipitation is present, the radar reflectivity and DVV profile pair is examined for the presence of a bright band using the technique described by White et al. (2002). If the fraction of profiles with precipitation present and a bright band is ≥0.5 mm, then the BB rain designation is assigned to the 30-min analysis period. Otherwise the NBB rain designation is assigned. BB rain is partitioned further objectively using these definitions: "cold" rain does not exhibit a downward increase in reflectivity below the bright band, while "hybrid" rain (as described in section 1) does exhibit a downward increase (≥0.1 dB) in reflectivity below the bright band. We use the term hybrid because the existence of a bright band indicates that ice processes are contributing to the precipitation, while the increase in reflectivity below the bright band indicates growth by collision and coalescence (i.e., warm rain processes).

After a winter season's dataset is run through this automated algorithm, visual inspection is conducted and two additional designations are assigned. If a period was labeled as NBB rain, but it is evident from the S-PROF data and other measurement sources that the precipitation is convective in nature, then the period is relabeled "convection." In convection, a melting layer may be present, but the enhanced vertical motion and turbulence in convection can disrupt the structure of this layer such that a bright band is not easily detected. In other NBB-designated cases, the bright band may descend below the minimum detectable range of the radar. These periods are relabeled with the designation "BB too low," indicating that either the BB is lower than the minimum detectable range of the S-PROF or snow is descending all the way to the surface. This situation is diagnosed using collocated surface temperature measurements and, when applicable, the temporal continuity of the brightband time–height series when it drops below the lowest radar range gates during its descent toward the surface or when it rises above the lowest radar range gates during its ascent from the surface. When the S-PROF is collocated with an optical disdrometer (see section 3a), data from the disdrometer are also used to determine the phase of precipitation because the instrument measures both the size and fall velocity of the hydrometeors.

Table 1 lists the 13 S-PROF deployments in the western United States that have archived data available for the multiwinter analysis presented here. Most of these deployments were associated with specific field campaigns and are therefore episodic. The only site that has provided a longer-term record is CZD, where data for 15 cool seasons have been collected to date. Figure 2 is a terrain map that identifies the locations of these S-PROF deployments. All of the datasets used in this study have been analyzed by the same two scientists using the methods described in section 2 to ensure consistency in the results.

Figure 3 lists the annual percentage and site-average percentage of wintertime rainfall that has been

TABLE 1. Locations, elevations, and periods of operation of the 13 S-PROFs that provided data between 1998 and 2014 for the rainfall process partitioning analyses presented in this study.

Location	Station ID	Lat (°N)	Lon (°W)	Elev (m)	Start date	End date
Cazadero, CA	CZD	38.61	123.21	475	1 Jan 1998	31 Mar 1998
					12 Jan 2001	8 Mar 2001
					16 Dec 2001	6 Apr 2002
					9 Dec 2002	9 Apr 2003
					13 Dec 2003	21 Mar 2004
					11 Nov 2004	1 Apr 2005
					16 Nov 2005	25 Apr 2006
					1 Dec 2006	30 Apr 2007
					21 Nov 2007	9 Apr 2008
					8 Nov 2008	9 May 2009
					6 Nov 2009	11 May 2010
					2 Nov 2010	31 Mar 2011
					16 Nov 2011	1 May 2012
					13 Dec 2012	16 Apr 2013
					6 Nov 2013	1 Apr 2014
Bodega Bay, CA	BBY	38.31	123.07	12	12 Jan 2001	8 Mar 2001
					9 Dec 2003	20 Mar 2004
Grass Valley, CA	GVY	39.17	121.11	689	17 Jan 2002	8 Apr 2002
Mackenzie Bridge, OR	MBO	44.18	122.09	512	15 Nov 2001	13 Jan 2002
Alta, CA	ATA	39.20	120.82	1085	1 Dec 2005	25 Apr 2006
					26 Oct 2006	30 Apr 2007
					15 Nov 2007	25 Mar 2008
					18 Nov 2008	28 Apr 2009
Colfax, CA	CFC	39.08	120.94	644	15 Nov 2007	22 Apr 2008
Point Sur, CA	PTS	36.30	121.89	10	30 Oct 2008	14 Apr 2009
Sugar Pine, CA	SPD	39.13	120.80	1066	20 Feb 2009	28 Apr 2009
					11 Nov 2009	30 Apr 2010
					7 Nov 2010	12 Apr 2011
					17 Nov 2011	1 May 2012
					1 Nov 2012	15 Apr 2013
Mariposa, CA	MPI	37.51	120.04	610	5 Dec 2009	28 Apr 2010
					1 Dec 2010	15 Mar 2011
Westport, WA	WPT	46.91	124.11	5	16 Oct 2009	17 May 2010
					25 Oct 2010	25 Apr 2011
					1 Oct 2011	31 May 2012
					29 Nov 2012	10 Apr 2013
Ravensdale, WA	RVD	47.31	121.85	301	13 Nov 2009	17 May 2010
					14 Oct 2010	26 Apr 2011
Davis, CA	DVS	38.58	121.86	30	9 Feb 2012	30 Apr 2012
					9 Oct 2012	16 Apr 2013
Santa Rosa, CA	STR	38.51	122.80	40	9 Feb 2012	30 Apr 2012
					10 Oct 2012	16 Apr 2013
					6 Nov 2013	29 Apr 2014

attributed to the NBB rain category for all of the S-PROF deployments. Table 2 lists these annual percentages along with annual accumulations of NBB rain for CZD, SPD, and MPI, the S-PROF sites of most interest to the current study. There is substantial interannual variability in the contribution from NBB rain, which is especially notable at the long-term observing site at CZD. Here, NBB rain has contributed as much as 50% and as little as 18% of the seasonal rainfall total. The cause of this variability has yet to be determined. Neiman et al. (2005) ruled out the phase of ENSO as a cause. The S-PROF observations in 2001 coincided with a particularly cold storm track with typically weak ARs (not shown). That season also had a minimum in the annual contribution of NBB rain at the two coastal S-PROF observing sites [Bodega Bay (BBY) and CZD]. Therefore, the seasonal storm track could be at least partially responsible for the observed interannual variability in the NBB rain contribution.

There is also significant spatial variability that is more statistically robust for sites that have more than one year of record. In particular, the two S-PROF sites

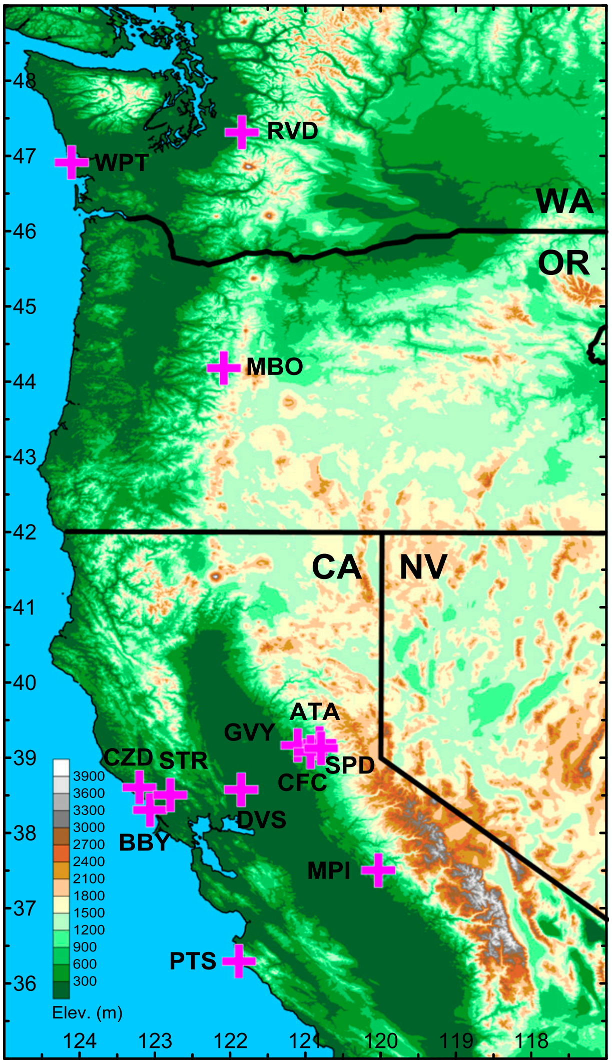

FIG. 2. Terrain base map showing the locations of the 13 sites where S-PROF deployments occurred between 1998 and 2014. The site names corresponding to the three-letter identifiers are given in Table 1.

in the Sierra Nevada supported by CalWater (MPI and SPD) experienced similar percentages of NBB rain from year to year, but the average contribution at SPD was nearly twice the average contribution at MPI. For the two years when the S-PROFs at both SPD and MPI were operating, SPD had more than twice the amount of NBB rain than MPI had (359.2 versus 148.6 mm). Furthermore, the average percentage of NBB rain at SPD is similar to the average percentage observed at CZD. Understanding this behavior is the major motivation for the case study presented in section 4. First, we present annual wet deposition data that provides initial evidence to suggest that SPD is influenced by maritime air during landfalling winter storms, whereas MPI is not.

4. Wet deposition of sea salt

Annual wet deposition maps of sodium and chloride ions in precipitation were acquired from the National Atmospheric Deposition Program (NADP) National Trends Network (NTN; http://nadp.sws.uiuc.edu/NTN/annualmapsByYear.aspx#2010). Deposition samples represent only wet deposition (i.e., aerosols removed from the atmosphere from precipitation through rainout, washout, or cloud particle nucleation) because the automatic collectors only open during precipitation events. In order for the NTN to generate these annual deposition maps, precipitation samples are collected at sites located away from pollution point sources by the NTN on a weekly basis (typically on Tuesday) to measure concentrations of specific soluble analytes. All samples are sent to the Central Analytical Laboratory at the Illinois State Water Survey for analysis, data entry, verification, and screening. Annual gradient maps of precipitation-weighted mean concentrations and deposition are available for NTN. The annual deposition maps (kg ha^{-1}) shown herein were generated by NTN using concentration and precipitation surface data and the Parameter-Elevation Relationships on Independent Slopes Model (PRISM; Daly et al. 1994). The PRISM precipitation estimates incorporate point observation data, a digital elevation model, and expert knowledge of complex climatic variables that result in high-resolution, continuous, digital grid estimates of total annual precipitation. The annual precipitation surfaces have a roughly 2.3-km spatial resolution.

The chemical composition of the precipitation falling near MPI versus SPD varied considerably, particularly species representative of sea salt (Creamean et al. 2014). Figure 4 shows the 2010 annual wet deposition of ions of sodium (Na^+) and chloride (Cl^-) in California. The year 2010 was chosen here because it encompasses the case study presented in section 5. Also, 2010 had the greatest number of days when S-PROF measurements were available from both SPD and MPI from any year between 2009 and 2011 (i.e., CalWater 1). Hence, the wet deposition results are most applicable to the rainfall process partitioning results from 2010. When comparing the regions surrounding both sites, wet deposition of both sodium and chloride ions was higher in the SPD region compared to MPI and is more similar to deposition observed along the Northern California coastal mountains. One plausible explanation is that SPD is often preferentially oriented downwind of AR flow through the SFBA gap during winter storms. In this case, the first significant obstacle the moist AR air mass would encounter is the northward moving layer of cool, stable air in the SBJ on the windward side of the Sierra Nevada. CalWater research has already shown that ARs often override the

Year	CZD	BBY	GVY	MBO	ATA	CFC	PTS	SPD	MPI	WPT	RVD	DVS	STR
1998	29.4												
2001	18.2	24.5											
2001/02	50.0		35.3	17.8									
2002/03	41.5												
2003/04	42.2	31.4											
2004/05	29.3												
2005/06	37.3				21.2								
2006/07	38.0				29.4								
2007/08	29.0				17.2	14.9							
2008/09	31.6				31.8[1]		26.3	38.8					
2009/10	26.4							32.8[3]	14.1	15.6	15.7[2]		
2010/11	30.6							27.2[4]	16.0	13.1	21.2		
2011/12	24.9							14.8		17.5		8.0	18.6
2012/13	21.3[5]							21.2		11.4[6]		15.3	26.8
2013/14	33.2												20.4
Average	**32.2**	**28.0**	**35.3**	**17.8**	**24.9**	**14.9**	**26.3**	**27.0**	**15.1**	**14.4**	**18.5**	**11.7**	**21.9**

FIG. 3. The percentage of NBB rain relative to total ascribed rainfall (BB + NBB + convective) during the winter seasons. The pie chart for each site displays the annual fractional accumulation of each rainfall type shown in the key.

SBJ (Kingsmill et al. 2013) and cause locally enhanced orographic precipitation (Neiman et al. 2013). Sea salt aerosols generated from strong winds and air–sea fluxes over the Pacific Ocean are presumably transported inland with the AR. The topography in the SFBA gap is minimal; orographically enhanced precipitation is not observed and thus is the cause of the dearth of sodium and chloride ion deposition in that location. Deposition south of the SFBA gap also is reduced as compared to north of the SFBA gap. This behavior mimics total precipitation observed during 2010 (not shown; analysis available from the Advanced Hydrologic Prediction Service).

The presence of sea salt ions at SPD is indicative of the influence of air masses from a marine origin, whereas air transported to MPI is less directly influenced from the Pacific Ocean because of upstream coastal orography. Further, the large influence from sea salt species in the precipitation surrounding SPD is collocated with larger amounts of NBB rain, compared to MPI. This suggests that the sea salt is either scavenged by falling precipitation (Rodhe and Grandell 1972) or possibly used to form cloud droplets by serving as large or giant cloud condensation nuclei (CCN), aiding the formation of NBB rain. Large or giant CCN (typically treated as >2 μm) are thought to result in an early development of large drops in the lower cloud layers (Posselt and Lohmann 2008; Rosenfeld et al. 2001; Yin et al. 2000). However, we cannot determine the extent to which sea salt aerosols were either scavenged or served as giant CCN.

Overall, the combination of greater deposition of sea salt species and enhanced NBB rain at SPD in comparison to MPI supports the hypothesis that ARs introduce moist, marine air from the Pacific Ocean to the northern Sierra Nevada in comparison to the south. To further investigate how California's coastal geography impacts precipitation in the Sierra Nevada, a case study is used in

TABLE 2. The amount and percentage of NBB rain relative to total ascribed rainfall (BB + NBB + convective) during the winter seasons listed in Fig. 3 and for the selected sites analyzed in this study.

	Amount (mm)			Percentage of ascribed (%)		
	CZD	SPD	MPI	CZD	SPD	MPI
1998	513.0			29.4		
2001	101.6			18.2		
2001/02	339.4			50.0		
2002/03	532.9			41.5		
2003/04	469.7			42.2		
2004/05	202.7			29.3		
2005/06	743.5			37.3		
2006/07	333.8			38.0		
2007/08	328.7			29.0		
2008/09	313.4	94.5		31.6	38.8	
2009/10	377.2	163.8*	73.2	26.4	32.8	14.1
2010/11	293.9	216.9**	75.4	30.6	27.2	16.0
2011/12	224.0	50.3		24.9	14.8	
2012/13	107.4	157.0		21.3	21.2	
2013/14	269.0			33.2		
Avg	343.3	124.6	74.3	32.2	27.0	15.1

* The subset value for SPD that corresponds to the period when MPI was operating is 153.7 mm.

** The subset value for SPD that corresponds to the period when MPI was operating is 205.5 mm.

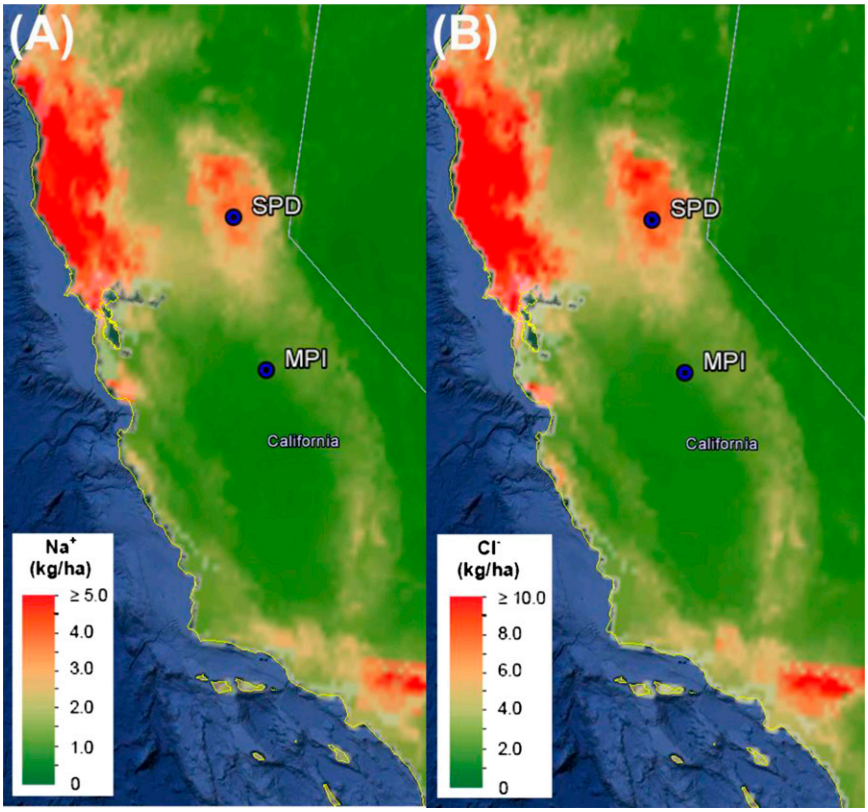

FIG. 4. NADP NTN 2010 annual wet deposition maps for (a) Na^+ and (b) Cl^- concentrations shown in Google Earth. The highest precipitation ion deposition is shown in red, while the lowest is shown in green. Locations of SPD and MPI are also shown. Data for maps were acquired from the NADP NTN website (http://nadp.sws.uiuc.edu/).

the following section to demonstrate the regional synoptic patterns and local mesoscale processes that ultimately control the observed bulk microphysical properties of the precipitation.

5. The case study of 23–25 February 2010

The storm that impacted northern and central California from 23 to 25 February 2010 was chosen because it has the characteristics that are common to many other winter storms. The two key ingredients are the presence of an AR and the SBJ. Furthermore, it was a fairly progressive storm, allowing for a direct comparison of meteorological forcing and resultant rainfall statistics observed at the two Sierra Nevada foothills observing sites (MPI and SPD) that are separated by a horizontal distance of 192 km.

a. Datasets used in the case study

Two operational weather satellites were used to provide a meteorological context for the case study period. We used the infrared imagery from the GOES constellation. *GOES-15*, located at 135°W, is the satellite in this constellation that currently provides images over the eastern Pacific Ocean. Prior to its decommissioning in December 2011, *GOES-11* fulfilled this role. The Special Sensor Microwave Imager/Sounder (SSM/IS) is a 24-channel, 21-frequency, linearly polarized passive microwave radiometer system. The instrument is flown on board the U.S. Air Force Defense Meteorological Satellite Program (DMSP) *F-16*, *F-17*, and *F-18* satellites. We used the IWV product from the SSM/IS satellites.

The ground-based instrumentation provided by HMT and CalWater is listed in Table 3. The 915-MHz wind profilers (Carter et al. 1995) provide continuous hourly averaged wind profiles from 180 m to ~4 km, at 60- or 100-m vertical resolution. Postexperiment data quality control is performed using the continuity method of Weber et al. (1993), followed by visual inspection to remove any remaining outliers. The vertically pointing precipitation profiler (S-PROF) was described in section 1. A precipitation disdrometer was collocated at each of the S-PROF sites. The Parsivel optical disdrometer uses a laser diode to produce a horizontal sheet of light

TABLE 3. HMT and CalWater instrumented sites that provided datasets used in the 23–25 Feb 2010 case study.

Location	Station ID	Lat (°N)	Lon (°W)	Elev (m)	Instrumentation
Berkeley, CA	SVC	37.86	122.22	407	GPS-Met
Bodega Bay, CA	BBY	38.31	123.07	12	Wind profiler, GPS-Met, 10-m meteorological tower
Cazadero, CA	CZD	38.61	123.21	475	S-PROF, 10-m meteorological tower
Chico, CA	CCO	39.70	121.91	42	GPS-Met
Chowchilla, CA	CCL	37.11	120.24	73	Wind profiler, GPS-Met, 10-m meteorological tower
Colfax, CA	CFC	39.08	120.94	644	Wind profiler, GPS-Met, 10-m meteorological tower
Concord, CA	CCR	37.99	122.06	5	Wind profiler, GPS-Met, 10-m meteorological tower
Dixon, CA	FFM	38.47	121.65	7	GPS-Met
Fort Bragg, CA	FBG	39.44	123.81	17	GPS-Met
Lost Hills, CA	LHS	35.62	119.69	80	Wind profiler, 10-m meteorological tower
Mariposa, CA	MPI	37.51	120.04	674	S-PROF, GPS-Met, 10-m meteorological tower
Morgan Hill, CA	LCD	37.10	121.65	72	GPS-Met
Oakdale, CA	WCC	37.80	120.64	83	GPS-Met
Petaluma, CA	MHL	38.30	122.74	91	GPS-Met
Pigeon Point, CA	PPT	37.19	122.39	42	GPS-Met
Placerville, CA	SMT	38.83	120.69	1079	GPS-Met
Planada, CA	PLD	37.35	120.20	96	GPS-Met
Point Arena, CA	PAN	38.93	123.73	21	GPS-Met
Redwood City, CA	MCK	37.47	122.36	434	GPS-Met
Sacramento, CA	SAC	38.30	121.42	6	Wind profiler
Sloughhouse, CA	SHS	38.49	121.21	60	Wind profiler, GPS-Met, 10-m meteorological tower
Sugar Pine Dam, CA	SPD	39.13	120.80	1066	S-PROF, 10-m meteorological Tower
Truckee, CA	TRK	39.32	120.14	1797	Wind profiler, GPS-Met, 10-m meteorological tower

30 mm wide, 180 mm long, and 1 mm high, providing a sampling volume of 5400 mm^3. When particles (e.g., precipitation) pass through the light sheet, a portion of the transmitted laser light is blocked and the voltage produced by the photodiode is reduced relative to when no particles are present in the beam. The amplitude of the voltage drop is related to the size of the particle. The amount of time it takes for the particle to pass through the sheet provides the particle's velocity. For the current study, only the size information is used. A new size distribution covering 32 size bins ranging from 0.062 to 24.5 mm was collected every 2 min. Surface meteorology variables (pressure, temperature, relative humidity, wind speed, wind direction, and solar and net radiation) were measured with commercially available, research-grade instruments (White et al. 2013) on a 10-m tower mast, and precipitation accumulation was measured with a Texas Electronics heated tipping-bucket gauge.

Through the HMT-Legacy project, newly installed or preexisting global positioning system (GPS) receivers across California were converted to GPS-Met receivers. To do this, surface meteorological equipment (pressure and temperature sensors) was added along with real-time data communications to allow the GPS receiver signals to be combined with GPS satellite orbit data to estimate the IWV in the column above the GPS antenna (Bevis et al. 1992; Duan et al. 1996; Gutman et al. 2004).

b. *Synoptic-scale context*

GOES infrared satellite imagery with 500-hPa geopotential height analyses (Fig. 5) provide synoptic-scale context for the case study. The 36-h period in Fig. 5 was characterized by a progressive baroclinic wave train over the eastern North Pacific. The cyclonic disturbance that subsequently impacted California was centered over the Gulf of Alaska at 1200 UTC 23 February (Fig. 5a), while a transient ridge axis was positioned over the state. A north–south cloud band embedded in southwesterly flow immediately offshore marked an organized region of warm advection at and below ~700 hPa (not shown). Twelve hours later (Fig. 5b), the southwesterly flow and associated warm-advection cloud band impacted California in advance of a progressive short-wave trough, while the 500-hPa cyclone center remained over the Gulf of Alaska. A shallower northeast–southwest cloud band extended offshore from California and marked a region of organized ascent ahead of an advancing lower-tropospheric (i.e., below ~700 hPa) polar cold front making landfall in southern Oregon (not shown). By 1200 UTC 24 February (Fig. 5c), the warm-advection cloud band and short-wave trough progressed inland and were decaying over the complex orography, while the flow aloft became more zonal. The cold-frontal cloud band was positioned across central California and over the adjacent coastal waters. At the end of the 36-h period (Fig. 5d), subsiding and comparatively cloud-free northwesterly flow covered California.

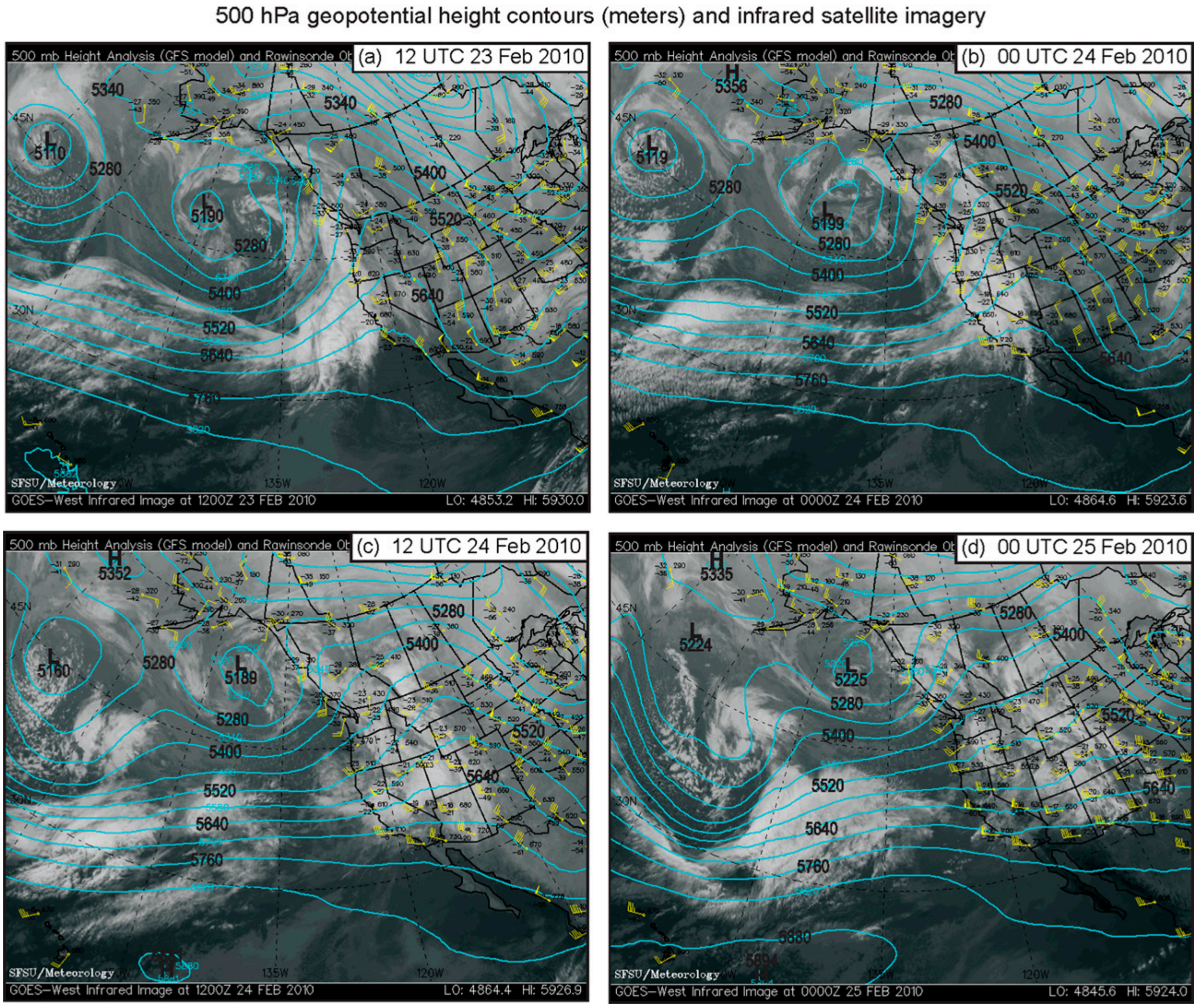

FIG. 5. The 500-hPa geopotential height analyses (m; contours) superimposed on infrared satellite images at (a) 1200 UTC 23 Feb, (b) 0000 UTC 24 Feb, (c) 1200 UTC 24 Feb, and (d) 0000 UTC 25 Feb 2010. Rawinsonde-observed wind velocities are shown in yellow (flags = 25 m s^{-1}; barbs = 5 m s^{-1}; half barbs = 2.5 m s^{-1}). Images were obtained from the Department of Geosciences' Meteorology Program at San Francisco State University.

Composite SSM/IS satellite images of IWV (Fig. 6) highlight the fact that an AR accompanied the landfalling short-wave trough and cold front on 23–25 February 2010. On the afternoon of 23 February (Fig. 6a), a long and narrow plume of enhanced IWV greater than 2 cm, indicative of AR conditions (e.g., Ralph et al. 2004; Neiman et al. 2008), extended northeastward from the southwestern edge of the domain toward the California coast. Twelve hours later (Fig. 6b), the core of the landfalling AR impacted the SFBA. By the afternoon of 24 February (Fig. 6c), the AR shifted equatorward beyond the San Francisco Bay and toward Southern California in response to the departing short-wave trough, cold front, and trailing subsidence.

c. Wind profiler and surface meteorology analyses

A detailed regional perspective is provided by the network of wind profilers across Northern California. We initially focus on time–height analyses of hourly wind-profiler data along the coast at BBY where terrain influences are typically modest, and then in California's Central Valley at Sloughhouse (SHS; Figs. 7 and 8) where the Sierra Nevada profoundly impacts the meteorology. Thereafter, we investigate key cross-sectional wind characteristics from the network (Fig. 9).

The time–height section of wind profiles and AR-parallel isotachs at BBY (Fig. 7a) shows the temporal descent of enhanced shear associated with an approaching

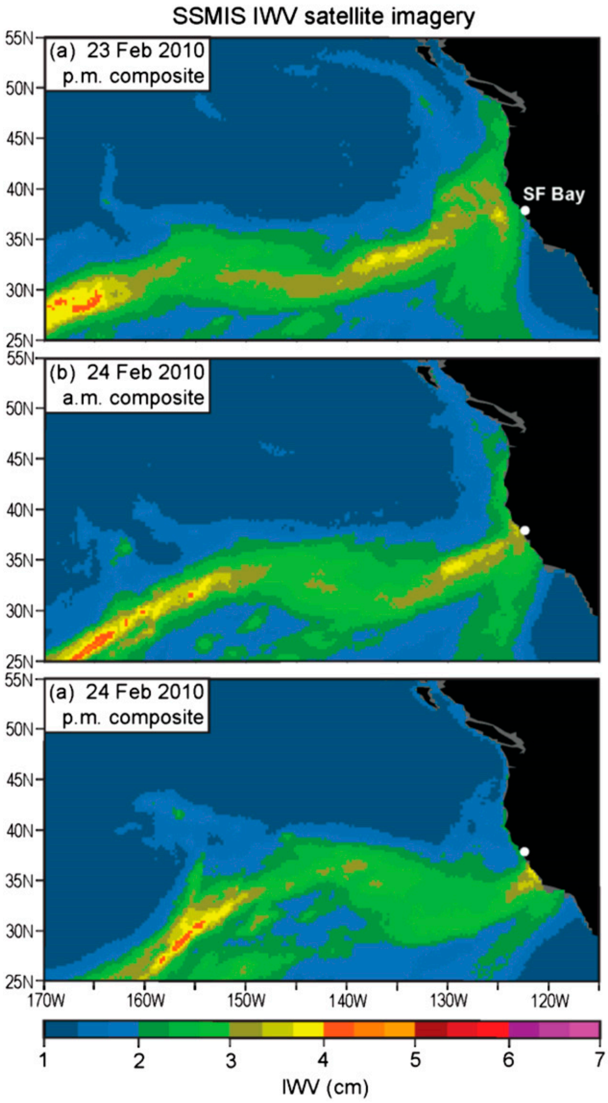

FIG. 6. Composite SSM/IS satellite images of IWV (cm; color scale at bottom) constructed from polar-orbiting swaths during the approximate periods between (a) 1330 and 1700 UTC 23 Feb ("p.m. composite"), (b) 0130 and 0500 UTC 24 Feb ("a.m. composite"), and (c) 1330 and 1700 UTC 24 Feb 2010 ("p.m. composite"). The location of the San Francisco Bay [labeled in (a) as "SF Bay"] is shown with a white dot.

warm front from 3–4 km above mean sea level (MSL) at ~0900 UTC 23 February to the surface at 0800 UTC 24 February. An axis of geostrophic warm advection [based on the thermal wind diagnostic in Neiman and Shapiro (1989)] coincided with the temporal descent of the approaching warm-frontal shear layer. The contiguous area of strong AR-parallel (>~16 m s^{-1}) southwesterly flow on the warm side of the warm front below ~3 km MSL coincided with IWV > 2 cm and marks the AR airstream. The AR-parallel isotachs also document the temporal ascent of the polar cold-frontal shear zone from the surface at ~0900 UTC 24 February to 3.8 km MSL at 1600 UTC 24 February. The cold front is marked by a wind shift from southwesterly to weaker northwesterly and geostrophic cold advection. Companion surface time series (Fig. 7b) generally show 1) warming, moistening, and decreasing pressure during the period of warm-frontal descent; 2) a pressure trough near the leading edge of the cold front; and 3) cooling, drying, and increasing pressure during the cold-frontal passage. The IWV exceeded the 2-cm threshold for AR conditions (e.g., Ralph et al. 2004) for ~21 h starting at 1400 UTC 23 February, and it subsequently decreases below the threshold with the cold-frontal passage. The companion time series of bulk IWV flux aligned with the AR [i.e., the product of IWV and the AR-parallel flow in the coastal orographic controlling layer between 0.75 and 1.25 km MSL, as in Neiman et al. (2002)] shows a sharp, narrow maximum exceeding the 25 m s^{-1} cm threshold for AR conditions (e.g., Neiman et al. 2009) immediately preceding the cold front. Rainfall (totaling 36.6 mm) fell primarily during and prior to the flux maximum and coincident with the warm-frontal descent toward the surface at BBY (i.e., the approaching warm front).

We believe that for this particular case, the period of maximum precipitation was dominated by isentropic lift associated with the approaching warm front. More typically, however, the heaviest precipitation in California's coastal mountains and Sierra Nevada is tied to orographic forcing. For example, Neiman et al. (2013) found that precipitation rate and IWV flux were highly correlated at zero lag (correlation coefficient 0.93–0.96) for a 13-case composite analysis observed at two stations in the northern Sierra Nevada and one in the Trinity Alps. This behavior is consistent with earlier results by Neiman et al. (2002) that showed a similarly high correlation between the upslope wind speed (i.e., the same component used in calculating the IWV flux) and orographic rainfall intensity observed in three different coastal mountain ranges.

The Central Valley time–height analysis from SHS (Fig. 7c) also shows the warm-frontal descent (during which the brightband melting level increased in altitude by ~1.5 km) and subsequent cold-frontal passage, but there are also key differences between SHS and BBY due to the impact of airflow blocking by the Sierra Nevada in the Central Valley. At SHS a strong south-southeasterly SBJ, with a core magnitude of 20–25 m s^{-1}, was situated between 300 and 1200 m MSL from 0000 to 1300 UTC 24 February. The blocked southerly component flow weakened and became shallower thereafter but persists until ~0000 UTC 25 February. The SBJ prevented the downward penetration of the warm front to the surface. Aloft, the cold-frontal wind shift (from southwesterly to

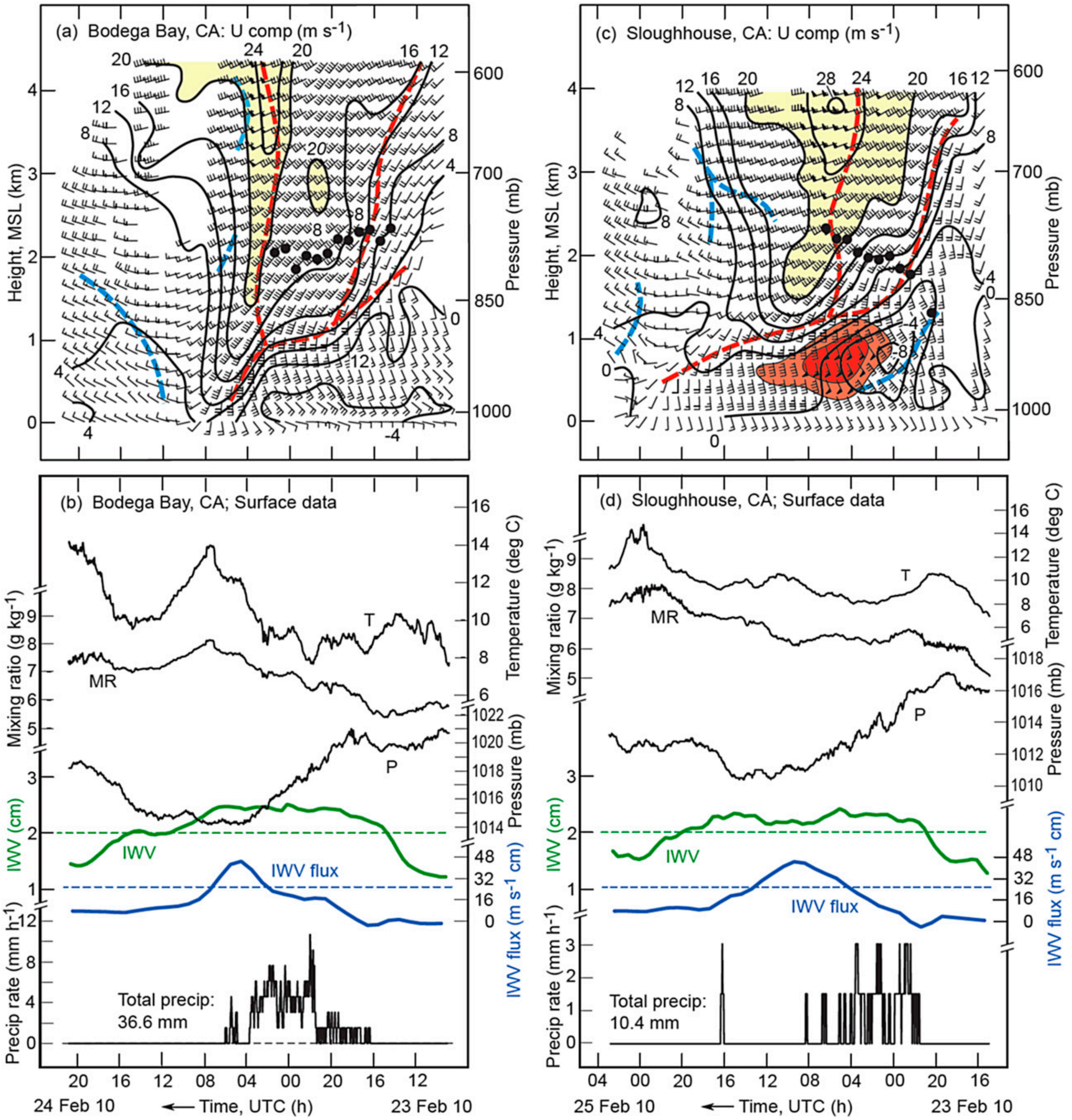

FIG. 7. Time series of observations from (left) BBY between 0900 UTC 23 Feb and 2100 UTC 24 Feb 2010 and (right) SHS between 1500 UTC 23 Feb and 0300 UTC 25 Feb 2010. Time increases from right to left to portray the advection of transient synoptic features from west to east. (a) Time–height section from BBY of hourly averaged wind profiles (flags and barbs are as in Fig. 5), AR-parallel (from 250°) isotachs (m s^{-1}; black contours with values >20 m s^{-1} shaded yellow), brightband melting-level heights (boldface black dots), and axes of max thermal wind–derived (i.e., geostrophic) warm and cold advection (red and blue dashed lines, respectively). Every wind profile and every other range gate is plotted. (b) Time series from BBY of surface temperature T, surface water vapor mixing ratio MR, surface pressure P, IWV (green), AR-parallel (i.e., from 250°) IWV flux (blue) in the coastal orographic controlling layer (0.75–1.25 km MSL), and 10-min averaged hourly rain rate (mm h^{-1}). The total precipitation accumulation (mm) is also given. The horizontal dashed green and blue lines mark the AR thresholds for the IWV and IWV flux, respectively (Ralph et al. 2004; Neiman et al. 2009). (c) As in (a), but for Sierra Nevada–parallel (from 160°) isotachs greater than 20 m s^{-1} (m s^{-1}; medium red shading, 20–24 m s^{-1}; dark red shading, >24 m s^{-1}). (d) As in (b), but for SHS, which utilizes a higher orographic controlling layer (1.25–1.75 km MSL) for the IWV flux impacting the Sierra Nevada.

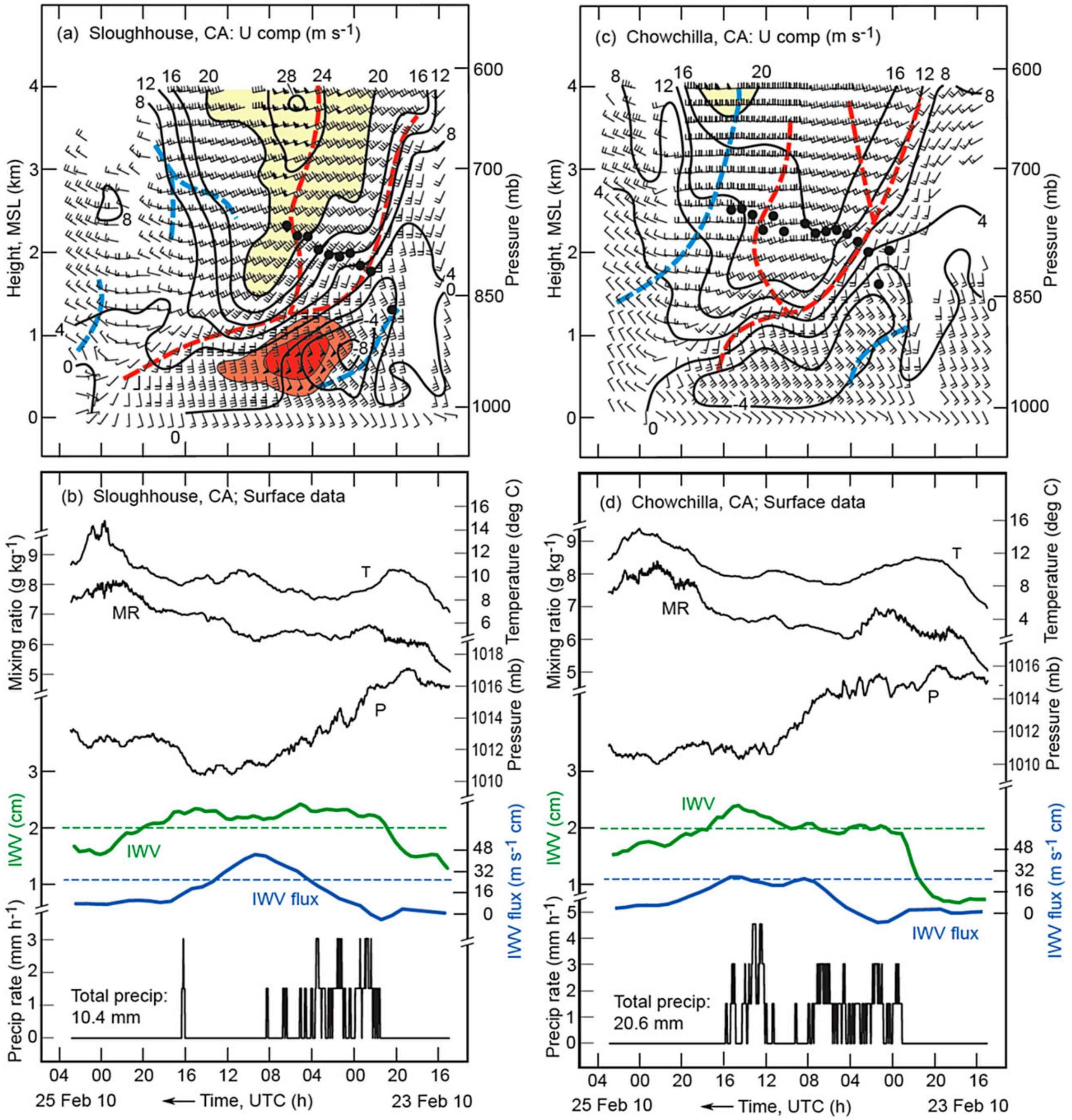

FIG. 8. Time series of observations between 1500 UTC 23 Feb and 0300 UTC 25 Feb 2010 from (a),(b) SHS and (c),(d) CCL. The setup is as in Fig. 7, with the exception that there is no red shading in (c) (i.e., the Sierra Nevada–parallel flow does not exceed 20 m s^{-1}).

northwesterly) and associated cold advection remained above the blocked flow, likely due to enhanced stable stratification in the SBJ. Hence, the cold front's interaction with the SBJ takes on the appearance of a terrain-forced, warm-frontal occlusion (e.g., Bergeron 1937). Despite the fact that IWV decreased steadily after 1500 UTC 24 February in response to post-cold-frontal drying aloft following the surface pressure trough, the surface temperature and mixing ratio continued to increase (Fig. 7d) because of the northward transport of heat and moisture from the SBJ, thus mirroring composite SBJ behavior in Neiman et al. (2013). The surface temperature and mixing ratio finally started declining at ~0000 UTC 25 February in response to colder post-cold-frontal flow aloft mixing down to the surface. The time series of bulk IWV flux at SHS (Fig. 7d)

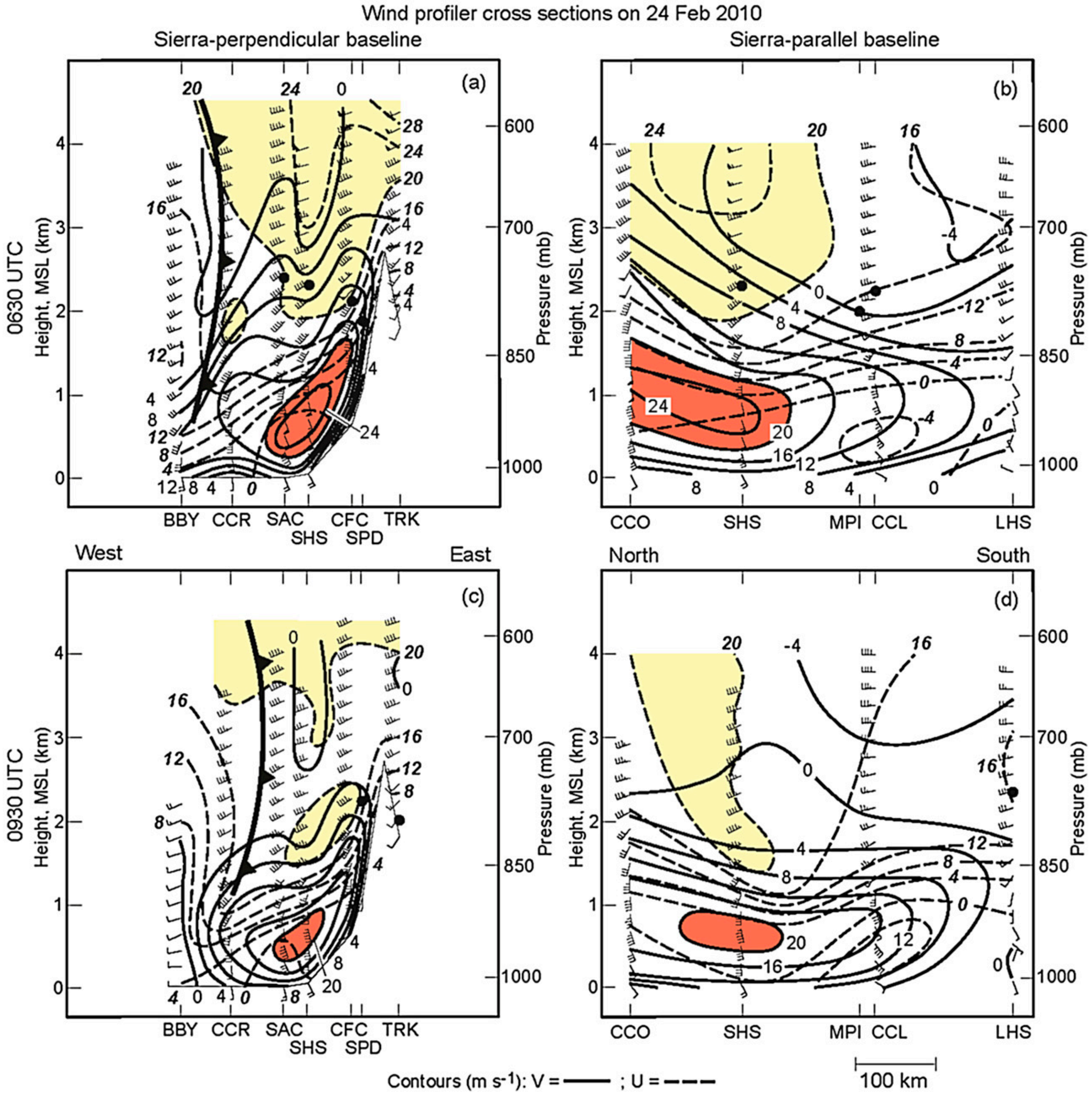

FIG. 9. Cross sections (see Fig. 1) of wind-profiler and S-PROF observations oriented (left) perpendicular and (right) parallel to the Sierra Nevada at (a),(b) 0630 UTC and (c),(d) 0930 UTC 24 Feb 2010. Solid black contours are the Sierra Nevada–parallel (from 160°) isotachs V (m s^{-1}; red shading, >20 m s^{-1}), and the dashed black contours are the AR-parallel (from 250°) isotachs U (m s^{-1}; yellow shading, >20 m s^{-1}). Brightband melting-level heights are depicted with boldface black dots. The cold front is shown using standard notation.

[where the orographic controlling layer is ~0.5 km higher than for the coastal mountains because of the larger-scale height of the Sierra Nevada (see, e.g., Neiman et al. 2013)] shows similar characteristics to its counterpart at BBY, although the peak is broader. Light rainfall at SHS (totaling ~10 mm) was confined largely to the warm-frontal SBJ period, although much heavier precipitation fell in the adjacent Sierra Nevada (e.g., ~60 mm at SPD).

Comparing the detailed atmospheric structures and evolutions observed by the wind profilers at SHS and Chowchilla (CCL) in the northern and southern Central Valley, respectively (Fig. 8), provides additional key information during the landfalling storm. In general, the synoptic and terrain-induced features (e.g., the warm and cold fronts, AR, and SBJ) were present at both sites. However, significant differences are also apparent. The cold front is ~8 h later at CCL, and the prefrontal southwesterly AR flow is weaker there. Also, the south-southeasterly SBJ flow was weaker at CCL, and it mixed out more quickly following the cold-frontal passage aloft. Finally, the bulk upslope IWV flux was ~50% weaker at CCL; hence, the orographic forcing was weaker at that site.

The wind-profiler cross sections (Fig. 9) provide additional regional perspective. The Sierra Nevada–perpendicular section at 0630 UTC 24 February (Fig. 9a) shows strong southwesterly, pre-cold-frontal AR flow exceeding 20 m s^{-1} overriding the shallow, south-southeasterly SBJ flow of 20–26 m s^{-1} less than 1 km above the Sierra Nevada's windward slope. The western edge of the SBJ resided within the Central Valley to the east of Concord (CCR), as was also documented in another case study and in a composite study (Kingsmill et al. 2013; Neiman et al. 2013). The brightband melting level is ~600 m lower over the Sierra Nevada foothills relative to its upwind elevation of ~2.4 km MSL over the Central Valley. Similar melting-level gradients were first noted over the Sierra Nevada by Marwitz (1983, 1987) and more recently over the windward slopes of the Italian Alps and Oregon Cascades (Medina et al. 2005). The physical processes driving this gradient (i.e., spatial variations in latent cooling, adiabatic cooling, and melting distance of frozen hydrometeors) were diagnosed by Minder et al. (2011) and Minder and Kingsmill (2013) using numerical-model and idealized simulations. A companion Sierra Nevada–parallel cross section (Fig. 9b) shows the AR flow aloft over the northern Central Valley. Below, SBJ flow encompassed most of the Central Valley's length, although the flow became stronger and deeper from SHS northward. This poleward gradient might be attributable, at least in part, to low-level AR flow entering the SFBA gap from the open ocean and subsequently turning northward within the SBJ flow (Neiman et al. 2013) and to melting-induced cool air draining the canyons of the windward foothills (e.g., Steiner et al. 2003) and also turning northward within the SBJ flow. By 0930 UTC 24 February, the cold front progressed eastward toward the Sierra Nevada's windward slope (Fig. 9c), and the AR aloft and shallow SBJ both weakened. In addition, the SBJ became shallower. The Sierra Nevada–parallel cross section at 0930 UTC (Fig. 9d) also shows a weakening of both the AR and SBJ components of the flow.

TABLE 4. Rainfall process partitioning statistics for the 23–25 Feb 2010 event.

	Amount (mm)		Percentage of ascribed (%)	
	SPD	MPI	SPD	MPI
Storm total	58.67	29.46		
Ascribed	57.15	25.91		
BB (cold)	2.79	0.00	4.89	0.00
BB (hybrid)	23.88	19.56	41.78	75.49
NBB	27.43	6.35	48.00	24.51
Convection	0.00	0.00	0.00	0.00
BB too low	3.05	0.00	5.33	0.00

Table 4 lists the total precipitation that fell at the two Sierra Nevada foothill locations (SPD and MPI) during the 23–25 February 2010 storm along with the results from the rainfall process partitioning algorithm for the same period. The difference between the storm total accumulations and the ascribed accumulations are due to 30-min sampling periods when there was only one tip of the bucket. In these cases, the algorithm was not run, as described in section 3. Not only did the northern Sierra Nevada site have nearly twice as much precipitation during the event as did the southern Sierra Nevada site (58.7 versus 29.5 mm), but the northern site also had more than 4 times the amount of NBB rain than the southern site had (27.4 versus 6.4 mm). Furthermore, the fractional contribution of NBB rain to the total precipitation ascribed by the algorithm at the northern Sierra Nevada site was nearly twice as large as at the southern Sierra Nevada location (48.0% versus 24.5%). These differences will be examined further using additional observational datasets.

d. S-PROF and disdrometer analyses

Figures 10 and 11 show time–height cross sections of equivalent S-PROF radar reflectivity factor (hereafter referred to as radar reflectivity), rainfall type, and disdrometer drop size distributions from SPD and MPI, respectively. For illustrative purposes, the vertical extent of the lowest useable beam from the closest NWS operational scanning Doppler weather radar [Next Generation Weather Radar (NEXRAD)] is indicated. At both sites, the precipitating cloud layer resided mostly within the lowest 8 km MSL. As the subcloud layer saturated at the outset of the storm, precipitation eventually reached the surface, as evidenced by precipitation particles observed by the disdrometer starting at approximately 2200 UTC 23 February at SPD (Fig. 10) and 0000 UTC 24 February at MPI (Fig. 11). However, since the rainfall process partitioning algorithm requires $\geq$0.5 mm of precipitation to fall within the 30-min sampling period, algorithm results are not available from MPI (Fig. 11) until 0530 UTC 24 February. At SPD (Fig. 10), which is farther north and higher in elevation than MPI (see Table 3), the precipitation started out as mix of rain and wet snow. As explained in section 3, the rainfall designation for these periods is subjectively labeled as "BB too low." As the cold subcloud layer at SPD is warmed by thermal advection, vertical mixing, and/or some other mechanism, the precipitation changes over to all rain.

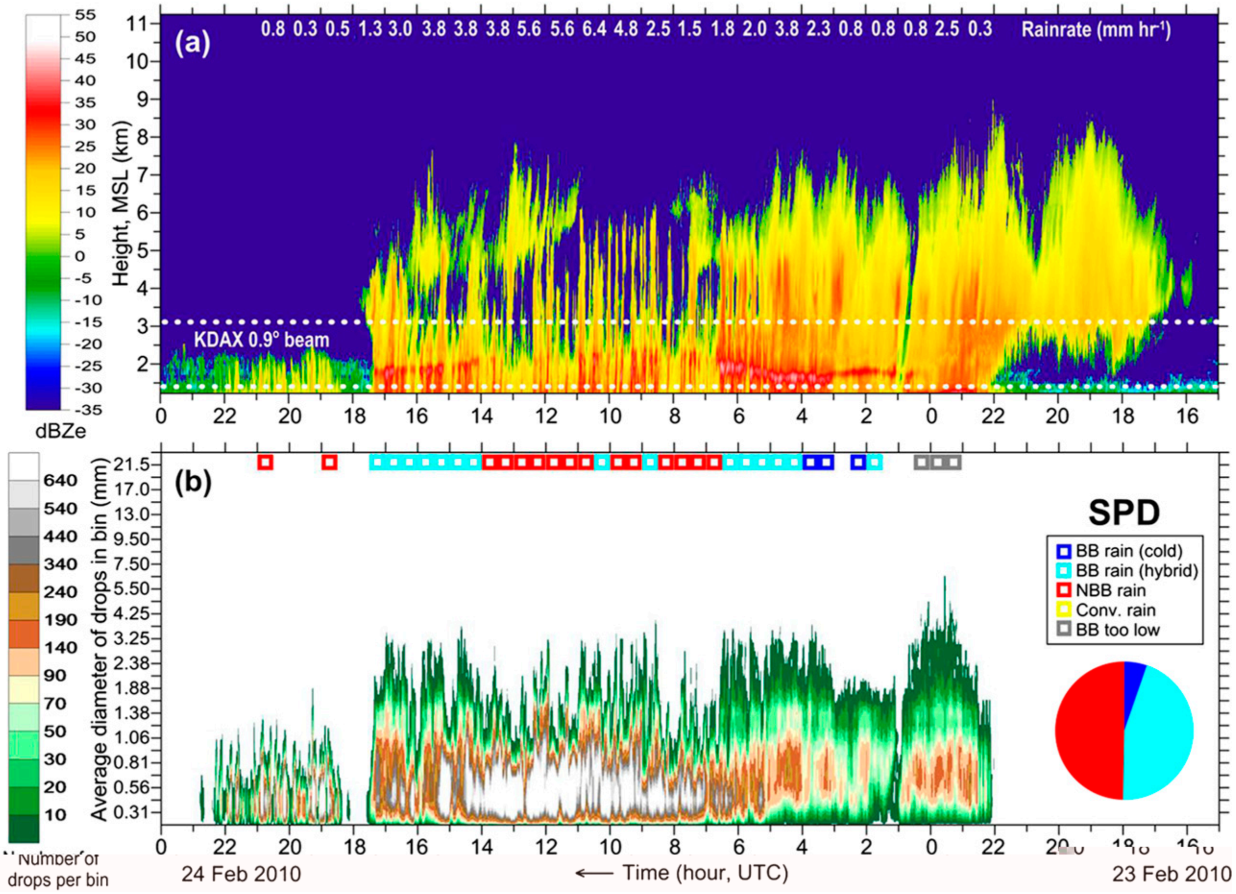

FIG. 10. (a) Time–height cross section of S-PROF equivalent radar reflectivity factor (dBZ_e) collected from 1500 UTC 23 Feb to 0000 UTC 25 Feb 2010 at SPD. The vertical extent of the lowest useable beam from NEXRAD at Davis, California, is indicated by the dashed white lines. The hourly rain rates (mm) are listed along the upper x axis. (b) Time–size cross section of disdrometer drop size distributions collected for the same period and location. The 30-min rainfall type designations resulting from the rainfall process partitioning algorithm are indicated by the key and open squares along the upper x axis. The relative contributions of each rainfall type (excluding ‘‘BB too low’’) are indicated by the pie chart. Time proceeds from right to left on all lower x axes.

Aside from the brief period of mixed precipitation at SPD, the precipitation at both sites started out as BB rain, as determined by the rainfall process partitioning algorithm and the unambiguous presence of a bright band in the S-PROF radar reflectivity profiles. This is an indication of the seeder–feeder orographic precipitation process (Bergeron 1965). The range of rain rates observed at each site during BB rain periods are comparable, perhaps because the seeder (upper) portion of the cloud was forced by large-scale ascent. At both sites, the brightband melting layer is also contained within the NEXRAD beam. The enhanced layer of radar reflectivity associated with the bright band will bias high the NEXRAD rainfall retrieval. This illustrates one of the challenges of using scanning radar reflectivity to estimate rainfall, although much research has occurred into adjusting the NEXARD rainfall retrieval for the shape of the vertical profile of reflectivity (e.g., Bellon et al. 2007; Matrosov et al. 2007; Zhang and Qi 2010).

Eventually, the upper portion of the precipitating cloud layer was removed, as the large-scale uplift associated with the storm left the immediate area, and primarily NBB rain ensued. This transition from BB to NBB rain occurred at 0630 UTC 24 February at SPD (Fig. 10) and 8 h later at 1430 UTC 24 February at MPI (Fig. 11). After this transition, MPI experienced NBB rain for the rest of the event. SPD had a mixture of BB and NBB rain and then transitioned back to all BB rain. BB rain can occur intermittently in a period of predominantly NBB rain, as was the case at SPD from 0830 to 9000 UTC and 1000 to 1030 UTC (Fig. 10), or vice versa, because the algorithm uses a simple majority of profiles collected during the 30-min sampling period to

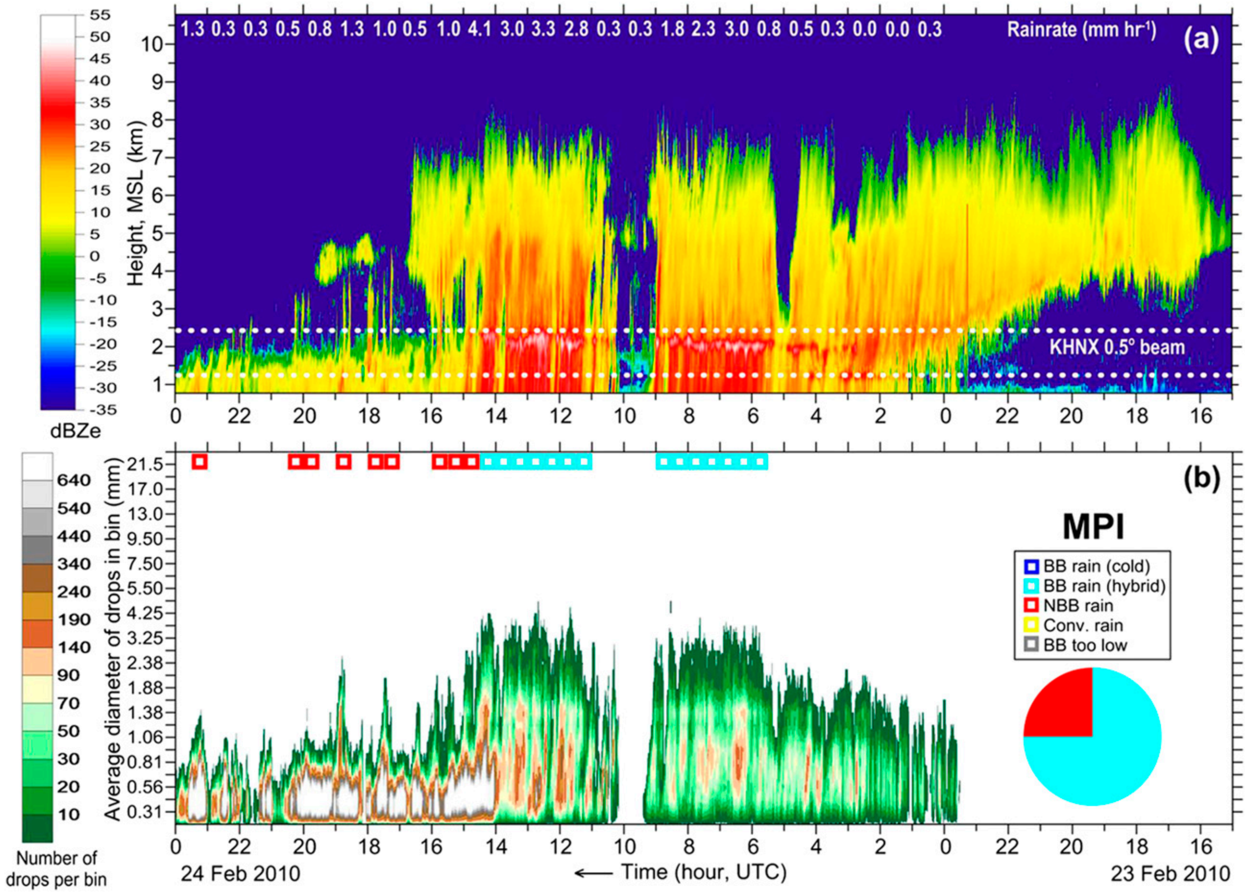

FIG. 11. As in Fig. 10, but for datasets collected at MPI. In this case, the closest NEXRAD (KHNX) is located at Hanford, California.

distinguish between the two types of rain. Within the 30-min sampling periods, multiple rainfall processes can occur in tandem, for example, hybrid rain, or alternating in rapid succession. For example, at SPD during the period of predominantly NBB rain from 0630 to 1400 UTC, there were intermittent periods of deeper ascent each lasting only a few minutes or less that produced rain showers, some of which contained a bright band.

As evidenced by the disdrometer data, NBB rain is characterized by a drop size distribution that is heavily weighted to many smaller (<~1mm) drops. Still, NBB produced the heaviest rain rates during the storm at SPD, while not at MPI. As described above, much of these differences are explained by the meteorological forcing. The orographic forcing diagnosed from the wind-profiler and GPS water vapor data (Fig. 8) is weaker at CCL (assuming to be representative of MPI) than at SHS (assuming to be representative of SPD). Both sites were dominated by the two rainfall designations (hybrid and NBB) that, when considered together, at least plausibly indicate the importance of collision–coalescence processes.

e. GPS horizontal IWV distribution

Another way to contrast the relative impacts of the AR as it passed by each site is to show a set of regional GPS-derived IWV maps every 4 h from 1200 UTC 23 February to 0000 UTC 25 February (Fig. 12). The IWV values are 30-min averages ending at the time listed at the top of each map.

The two GPS-Met stations located in the Central Valley upwind of SPD (enclosed in a rectangle in Fig. 12) indicate slightly larger values of IWV than the two GPS-Met stations located in the Central Valley upwind of MPI (enclosed in an oval in Fig. 12). For example, the maximum IWV occurring upwind of SPD at 0400 UTC 24 February was 2.4–2.6 cm, while the maximum IWV occurring upwind of MPI at 0800 UTC 24 February was 2.2–2.4 cm. This difference occurred even though the largest IWV values (2.6–2.8 cm) were observed on the coast upwind of MPI, while the values at the coast upwind of SPD are similar to those observed at SPD. This suggests that the coastal range upwind of MPI may have caused rainout and removal of some of the moisture in the AR as it crossed

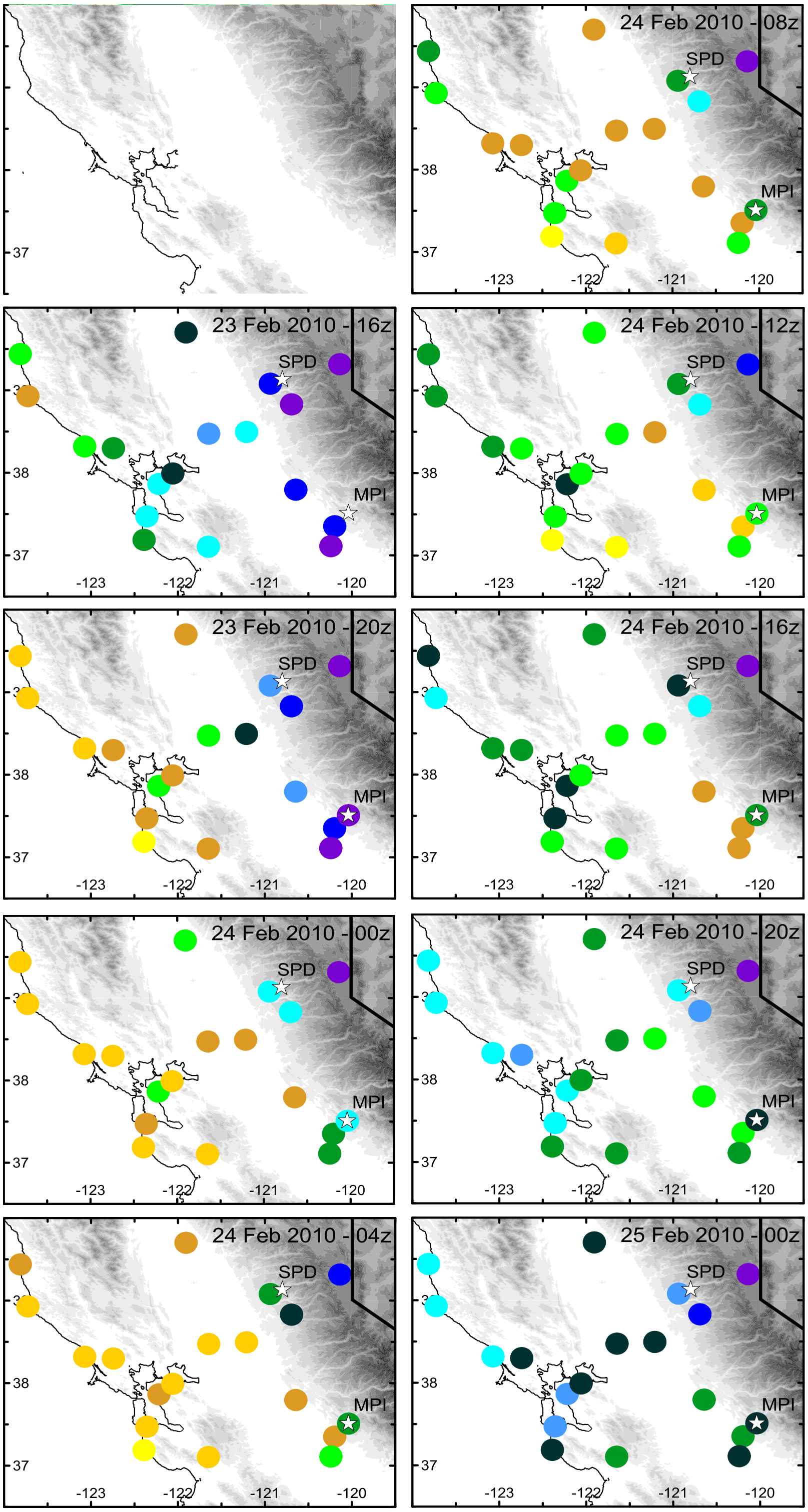

37
38
23 Feb 2010 - 16z
23 Feb 2010 - 20z
24 Feb 2010 - 00z
24 Feb 2010 - 04z
24 Feb 2010 - 08z
24 Feb 2010 - 12z
24 Feb 2010 - 16z
24 Feb 2010 - 20z
25 Feb 2010 - 00z
SPD
MPI
-123
-122
-121
-120

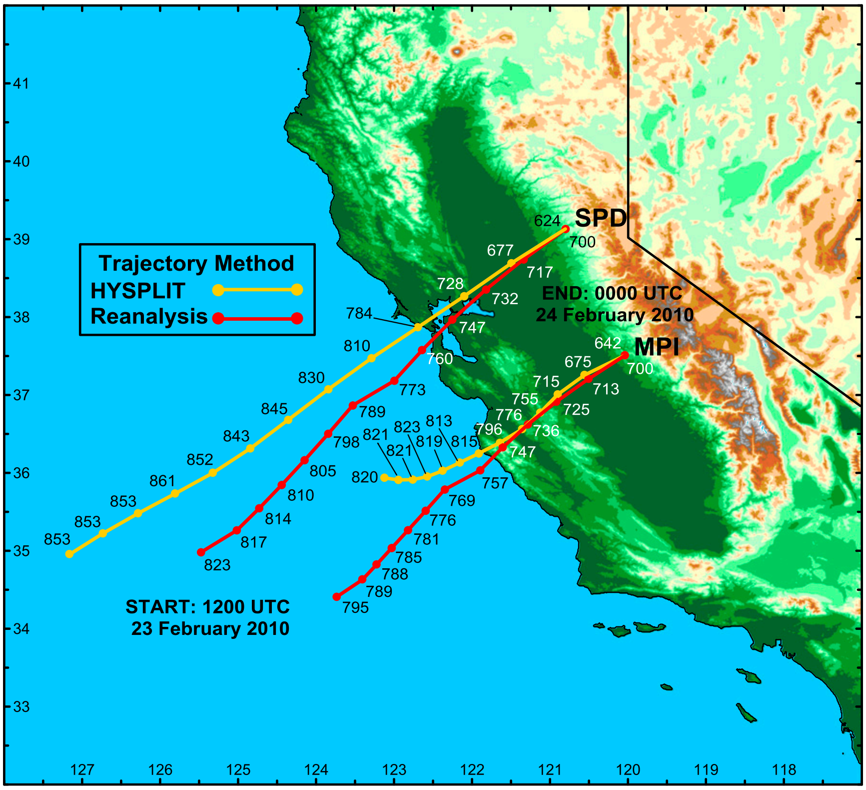

FIG. 13. The 12-h airmass parcel back trajectories arriving at SPD and MPI at 0000 UTC 24 Feb 2010 calculated using two different methods shown in the key (see text for more detail on each trajectory method). Each dot represents an hourly position along the trajectory, and the pressure level (hPa) at each position is also noted.

that part of the California coast, whereas the gap in coastal terrain upwind of SPD allowed relatively unimpeded maritime air in the AR to arrive at SPD.

One of the criteria that have been used to identify ARs over the ocean is an IWV content ≥2 cm (Ralph et al. 2004). The two GPS sites in the Central Valley closest to and upwind of SPD meet this AR criterion for a longer period (see rectangles; 16 h, i.e., from 0000 to 1600 UTC 24 February) than the two GPS sites farther south and upwind of MPI (see ovals; 12 h, i.e., from 0400 to 1600 UTC 24 February). The IWV observations at the SHS and CCL wind-profiler sites mirror this behavior. This means that the SPD site is exposed to AR conditions longer than MPI, which may further suggest that the gap in terrain afforded by the SFBA gap along with the additional confluence and convergence of moisture produced as flow in the AR encounters the SBJ allows the landfalling ARs to provide enhanced meteorological forcing for orographic precipitation at SPD as opposed to MPI.

f. Airmass trajectories

To determine if the GPS-Met IWV analysis indicates a preferred corridor of water vapor transport through the SFBA gap for this case study, we employed two different trajectory methods to determine where the air mass had traveled during the 12 h prior to arriving at SPD or MPI: HYSPLIT and reanalysis. HYSPLIT is described by Draxler and Hess (1997, 1998). We computed HYSPLIT trajectories using the Global Data Assimilation System, that is, the system that assimilates observed data into NOAA's Global Forecast System. The reanalysis trajectories were calculated from the NCEP–NCAR reanalyses using the web-based trajectory tool developed by the NOAA Physical Sciences Division (available at www.esrl.noaa.gov/psd/cgi-bin/data/trajtool/traj.pl). The trajectory algorithm used with this tool is from the University of Melbourne (Noone and Simmonds 1999). For the reanalysis trajectory method, we specified 700 hPa as the level at the trajectory endpoint, in part, to help ensure the trajectories did not intersect the ground before arriving at SPD, the higher of the two S-PROF sites. For HYSPLIT, the trajectory endpoint is specified as an altitude, so we chose 3000 m.

Analyzed back trajectories using the two methods are shown in Fig. 13. Both trajectory methods indicate airflow passing through a portion of the SFBA gap approximately

2–3 h before arriving at SPD. These methods also indicate flow passing over significant coastal mountain terrain approximately 3–4 h before arriving at MPI. These results further support the hypothesis that in this case and presumably others, moist airflow in ARs can penetrate inland through the SFBA gap and impact precipitation processes at SPD, whereas airflow arriving at MPI is influenced by upstream terrain, as further suggested by the annual wet deposition results (Fig. 4). Alexander et al. (2015) conducted a more in-depth, statistically based analysis of pathways that flow in ARs take in order to impact inland regions of the western United States. The SFBA gap and the Burney gap near the northeastern end of the Central Valley combined to be one of the primary flow corridors identified that results in delivering AR flow and extreme precipitation to southern Idaho.

6. Summary

NBB rain is a shallow rainfall process driven by collision and coalescence. Previous studies have used S-PROF radars to identify this process and document its microphysical structure along the U.S. West Coast. NBB rain contains a drop size distribution that is heavily skewed toward smaller drops. Yet, NBB rain can still, on occasion, produce rain rates comparable to and even larger than the deeper, seeder–feeder type precipitation, which results in larger drops and a brightband melting layer (i.e., BB rain). These findings highlight the challenge of using operational scanning radars to estimate rainfall in this region.

The CalWater project supported the deployment of two S-PROF radars; one in the northern Sierra Nevada at SPD and the other in the southern Sierra Nevada at MPI. These two sites both experienced NBB rain during two CalWater field seasons, but the fractional contribution of NBB rain to total seasonal rainfall was more than twice as large, on average, at the northern site than at the southern site (32% versus 15% for consistent periods of S-PROF operation). The total amount of NBB rain that fell at these two locations during these same periods followed suit (359.2 mm at SPD versus 148.6 mm at SPD). In addition, the average seasonal percentage of NBB rain observed at SPD was similar to the average seasonal percentage observed in the coastal mountains north of San Francisco at CZD; the first barrier encountered by landfalling ARs. We have shown that these sites have similar NBB rain contributions because SPD is often oriented downwind of the gap in coastal terrain caused by the SFBA gap during landfalling ARs in winter storms. This gap allows moist low-level flow to penetrate inland and enhance the collision–coalescence process in the orographic feeder cloud produced by ascent over the Sierra Nevada. The average orientation of this flow results in producing heavier NBB and overall rainfall at SPD than at MPI. Wet deposition of sea salt also suggests that maritime air in the AR reaches the northern Sierra Nevada site, but not the southern Sierra Nevada site, particularly for the year analyzed.

We examined a case study from 23 to 25 February 2010 to determine specifically how meteorological conditions could impact the distribution of rainfall and, more specifically, the role of the SBJ and the inland penetration of an AR on modulating precipitation enhanced by the Sierra Nevada. This case was also selected because it was consistent with differences in the annual accumulations of NBB rain at SPD and MPI. The along- (i.e., SBJ) and cross-barrier (i.e., AR parallel) flows were both stronger and deeper at SPD than at MPI. The moisture provided by the AR that aids in the generation of orographic precipitation was more enhanced upwind of SPD than upwind of MPI. Airflow trajectories also confirmed that air arriving at SPD passed through the SFBA gap, whereas air arriving at MPI traversed significant coastal terrain. All of these factors led to a heavier precipitation event at SPD compared to MPI. Perhaps more surprising is that NBB contributed more than half (55%) of the storm total precipitation that fell at SPD, while only 25% at MPI.

The S-PROF and disdrometer data highlighted the very different microphysical properties of the shallow, NBB rain, as compared to its much deeper seeder–feeder (BB rain) counterpart. Even though NBB rain is dominated by small (<~1 mm) drops, NBB rain produced the heaviest hourly rain rates observed at SPD during the storm, while not at MPI. Similar behavior was also observed at a different northern Sierra Nevada site for a different period by Coplen et al. (2008). However, the rainfall at both sites was dominated by collision–coalescence processes operating in an orographic environment as demonstrated by the combined contribution of hybrid and NBB rainfall. Gaining a better understanding of the meteorological and microphysical processes governing orographic precipitation will be necessary to improve representation of precipitation in numerical weather prediction models (e.g., Jankov et al. 2009; Lin et al. 2013). Improved predictability of orographic precipitation could lead to beneficial changes in how water resources are managed throughout the western United States. NOAA research is embarking on additional projects in California, such as CalWater 2, and elsewhere to help accomplish these goals.

Acknowledgments. The authors acknowledge the highly skilled engineering and technical staff at NOAA's Physical Sciences Division, who built, deployed, operated, and maintained the instruments used in this study. We also thank the many groups and individuals in California, Oregon, and Washington who have provided facilities for the instrument deployments used in this study. We greatly appreciate David Kingsmill and Sergey Matrosov and two anonymous reviewers for their comments and insight that helped to greatly improve this manuscript. Partial funding for CalWater was provided by the California Energy Commission. J. Creamean was partially funded by the National Research Council Research Associateship Program.

REFERENCES

Alexander, M. A., J. D. Scott, D. Swales, M. Hughes, K. Mahoney, and C. Smith, 2015: Moisture pathways into the U.S. Intermountain West during heavy winter precipitation events. *J. Hydrometeor.,* doi:10.1175/JHM-D-14-0139.1, in press.

Ault, A. P., C. R. Williams, A. B. White, P. J. Neiman, J. M. Creamean, C. J. Gaston, F. M. Ralph, and K. A. Prather, 2011: Detection of Asian dust in California orographic precipitation. *J. Geophys. Res.,* **116,** D16205, doi:10.1029/2010JD015351.

Bellon, A., G. W. Lee, A. Kilambi, and I. Zawadzki, 2007: Real-time comparisons of VPR-corrected daily rainfall estimates with a gauge Mesonet. *J. Appl. Meteor. Climatol.,* **46,** 726–741, doi:10.1175/JAM2502.1.

Bergeron, T., 1937: On the physics of fronts. *Bull. Amer. Meteor. Soc.,* **18,** 265–275.

——, 1965: On the low-level redistribution of atmospheric water caused by orography. *Proc. Int. Conf. on Cloud Physics,* Tokyo, Japan, IAMAP/WMO, 96–100.

Bevis, M., S. Businger, T. A. Herring, C. Rocken, R. A. Anthes, and R. H. Ware, 1992: GPS meteorology: Remote sensing of the atmospheric water vapor using the global positioning system. *J. Geophys. Res.,* **97,** 15 787–15 801, doi:10.1029/92JD01517.

Carter, D. A., K. S. Gage, W. L. Ecklund, W. M. Angevine, P. E. Johnston, A. C. Riddle, J. Wilson, and C. R. Williams, 1995: Developments in UHF lower tropospheric wind profiling at NOAA's Aeronomy Laboratory. *Radio Sci.,* **30,** 977–1001, doi:10.1029/95RS00649.

Coplen, T. B., P. J. Neiman, A. B. White, J. M. Landwehr, F. M. Ralph, and M. D. Dettinger, 2008: Extreme changes in stable hydrogen isotopes and precipitation characteristics in a landfalling Pacific storm. *Geophys. Res. Lett.,* **35,** L21808, doi:10.1029/2008GL035481.

Creamean, J. M., and Coauthors, 2013: Dust and biological aerosols from the Sahara and Asia influence precipitation in the western U.S. *Science,* **339,** 1572–1578, doi:10.1126/science.1227279.

——, C. Lee, T. C. Hill, A. P. Ault, P. J. DeMott, A. B. White, F. M. Ralph, and K. A. Prather, 2014: Chemical properties of insoluble precipitation residues. *J. Aerosol Sci.,* **76,** 13–27, doi:10.1016/j.jaerosci.2014.05.005.

——, A. P. Ault, A. B. White, P. J. Neiman, F. M. Ralph, and K. A. Prather, 2015: Interannual variations in aerosol sources and their impacts on orographic precipitation over California's central Sierra Nevada. *Atmos. Chem. Phys. Discuss.,* **15,** 931–964, doi:10.5194/acpd-15-931-2015.

Daly, C., R. P. Neilson, and D. L. Phillips, 1994: A statistical topographic model for mapping climatological precipitation over mountainous terrain. *J. Appl. Meteor.,* **33,** 140–158, doi:10.1175/1520-0450(1994)033<0140:ASTMFM>2.0.CO;2.

Draxler, R. R., and G. D. Hess, 1997: Description of the HYSPLIT_4 modeling system. NOAA Tech. Memo. ERL ARL-224, NOAA Air Resources Laboratory, Silver Spring, MD, 24 pp. [Available online at www.arl.noaa.gov/documents/reports/arl-224.pdf.]

——, and ——, 1998: An overview of the HYSPLIT_4 modeling system of trajectories, dispersion, and deposition. *Aust. Meteor. Mag.,* **47,** 295–308.

Duan, J., and Coauthors, 1996: GPS meteorology: Direct estimation of the absolute value of precipitable water. *J. Appl. Meteor.,* **35,** 830–838, doi:10.1175/1520-0450(1996)035<0830:GMDEOT>2.0.CO;2.

Guan, B., N. P. Molotch, D. E. Waliser, E. J. Fetzer, and P. J. Neiman, 2010: Extreme snowfall events linked to atmospheric rivers and surface air temperature via satellite measurements. *Geophys. Res. Lett.,* **37,** L20401, doi:10.1029/2010GL044696.

Gutman, S. I., S. R. Sahm, S. G. Benjamin, B. E. Schwartz, K. L. Holub, J. Q. Stewart, and T. L. Smith, 2004: Rapid retrieval and assimilation of ground based GPS precipitable water observations at the NOAA Forecast Systems Laboratory: Impact on weather forecasts. *J. Meteor. Soc. Japan,* **82,** 351–360, doi:10.2151/jmsj.2004.351.

Jankov, I., J.-W. Bao, P. J. Neiman, P. J. Schultz, H. Yuan, and A. B. White, 2009: Evaluation and comparison of microphysical algorithms in WRF-ARW Model simulations of Atmospheric River events affecting the California Coast. *J. Hydrometeor.,* **10,** 847–870, doi:10.1175/2009JHM1059.1.

Kingsmill, D. E., A. B. White, P. J. Neiman, and F. M. Ralph, 2006: Synoptic and topographic variability of Northern California precipitation characteristics in landfalling winter storms observed during CALJET. *Mon. Wea. Rev.,* **134,** 2072–2094, doi:10.1175/MWR3166.1.

——, P. J. Neiman, B. J. Moore, M. Hughes, S. E. Yuter, and M. Ralph, 2013: Kinematic and thermodynamic structures of Sierra barrier jets and overrunning atmospheric rivers during a landfalling winter storm in Northern California. *Mon. Wea. Rev.,* **141,** 2015–2036, doi:10.1175/MWR-D-12-00277.1.

Lavers, D. A., R. P. Allan, E. F. Wood, G. Villarini, D. J. Brayshaw, and A. J. Wade, 2011: Winter floods in Britain are connected to atmospheric rivers. *Geophys. Res. Lett.,* **38,** L23803, doi:10.1029/2011GL049783.

Lin, Y., B. A. Colle, and S. E. Yuter, 2013: Impact of moisture flux and freezing level on simulated orographic precipitation errors over the Pacific Northwest. *J. Hydrometeor.,* **14,** 140–152, doi:10.1175/JHM-D-12-019.1.

Martner, B. E., S. E. Yuter, A. B. White, S. Y. Matrosov, D. E. Kingsmill, and F. M. Ralph, 2008: Raindrop size distributions and rain characteristics in California coastal rainfall for periods with and without a radar bright band. *J. Hydrometeor.,* **9,** 408–425, doi:10.1175/2007JHM924.1.

Marwitz, J., 1983: The kinematics of orographic airflow during Sierra storms. *J. Atmos. Sci.,* **40,** 1218–1227, doi:10.1175/1520-0469(1983)040<1218:TKOOAD>2.0.CO;2.

——, 1987: Deep orographic storms over the Sierra Nevada. Part I: Thermodynamic and kinematic structure. *J. Atmos. Sci.,* **44,** 159–173, doi:10.1175/1520-0469(1987)044<0159:DOSOTS>2.0.CO;2.

Matrosov, S. Y., K. A. Clark, and D. E. Kingsmill, 2007: A polarimetric radar approach to identify rain, melting-layer, and snow regions for applying corrections to vertical profiles of reflectivity. *J. Appl. Meteor. Climatol.,* **46,** 154–166, doi:10.1175/JAM2508.1.

——, F. M. Ralph, P. J. Neiman, and A. B. White, 2014: Quantitative assessment of operational weather radar rainfall estimates over California's northern Sonoma County using HMT-West data. *J. Hydrometeor.,* **15,** 393–410, doi:10.1175/JHM-D-13-045.1.

Medina, S., B. F. Smull, R. A. Houze Jr., and M. Steiner, 2005: Cross-barrier flow during orographic precipitation events: Results from MAP and IMPROVE. *J. Atmos. Sci.,* **62,** 3580–3598, doi:10.1175/JAS3554.1.

Minder, J. R., and D. E. Kingsmill, 2013: Mesoscale variations of the atmospheric snow line over the northern Sierra Nevada: Multiyear statistics, case study, and mechanisms. *J. Atmos. Sci.,* **70,** 916–938, doi:10.1175/JAS-D-12-0194.1.

——, D. R. Durran, and G. H. Roe, 2011: Mesoscale controls on the mountainside snow line. *J. Atmos. Sci.,* **68,** 2107–2127, doi:10.1175/JAS-D-10-05006.1.

Moore, B. J., P. J. Neiman, F. M. Ralph, and F. E. Barthold, 2012: Physical processes associated with heavy flooding rainfall in Nashville, Tennessee, and vicinity during 1–2 May 2010: The role of an atmospheric river and mesoscale convective systems. *Mon. Wea. Rev.,* **140,** 358–378, doi:10.1175/MWR-D-11-00126.1.

Neiman, P. J., and M. A. Shapiro, 1989: Retrieving horizontal temperature gradients and advections from single-station wind profiler observations. *Wea. Forecasting,* **4,** 222–233, doi:10.1175/1520-0434(1989)004<0222:RHTGAA>2.0.CO;2.

——, F. M. Ralph, A. B. White, D. E. Kingsmill, and P. O. G. Persson, 2002: The statistical relationship between upslope flow and rainfall in California's coastal mountains: Observations during CALJET. *Mon. Wea. Rev.,* **130,** 1468–1492, doi:10.1175/1520-0493(2002)130<1468:TSRBUF>2.0.CO;2.

——, B. E. Martner, A. B. White, G. A. Wick, F. M. Ralph, and D. E. Kingsmill, 2005: Wintertime nonbrightband rain in California and Oregon during CALJET and PACJET: Geographic, interannual, and synoptic variability. *Mon. Wea. Rev.,* **133,** 1199–1223, doi:10.1175/MWR2919.1.

——, F. M. Ralph, G. A. Wick, J. Lundquist, and M. D. Dettinger, 2008: Meteorological characteristics and overland precipitation impacts of atmospheric rivers affecting the west coast of North America based on eight years of SSM/I satellite observations. *J. Hydrometeor.,* **9,** 22–47, doi:10.1175/2007JHM855.1.

——, A. B. White, F. M. Ralph, D. J. Gottas, and S. I. Gutman, 2009: A water vapour flux tool for precipitation forecasting. *Proc. Inst. Civ. Eng. Water Manage.,* **162,** 83–94, doi:10.1680/wama.2009.162.2.83.

——, M. Hughes, B. J. Moore, F. M. Ralph, and E. S. Sukovich, 2013: Sierra barrier jets, atmospheric rivers, and precipitation characteristics in Northern California: A composite perspective based on a network of wind profilers. *Mon. Wea. Rev.,* **141,** 4211–4233, doi:10.1175/MWR-D-13-00112.1.

Noone, D., and I. Simmonds, 1999: A three-dimensional spherical trajectory algorithm. Research activities in atmospheric and oceanic modelling, No. 28, WMO/TD-942, H. Ritchie, Ed., World Meteorological Organization, 3.26–3.27.

Posselt, R., and U. Lohmann, 2008: Influence of giant CCN on warm rain processes in the ECHAM5 GCM. *Atmos. Chem. Phys.,* **8,** 3769–3788, doi:10.5194/acp-8-3769-2008.

Ralph, F. M., P. J. Neiman, and G. A. Wick, 2004: Satellite and CALJET aircraft observations of atmospheric rivers over the eastern North Pacific Ocean during the winter of 1997/98. *Mon. Wea. Rev.,* **132,** 1721–1745, doi:10.1175/1520-0493(2004)132<1721:SACAOO>2.0.CO;2.

——, and Coauthors, 2005: Improving short-term (0–48 h) cool-season quantitative precipitation forecasting: Recommendations from a USWRP Workshop. *Bull. Amer. Meteor. Soc.,* **86,** 1619–1632, doi:10.1175/BAMS-86-11-1619.

——, P. J. Neiman, G. A. Wick, S. I. Gutman, M. D. Dettinger, C. R. Cayan, and A. B. White, 2006: Flooding on California's Russian River: The role of atmospheric rivers. *Geophys. Res. Lett.,* **33,** L13801, doi:10.1029/2006GL026689.

——, and Coauthors, 2013a: The emergence of weather-related test-beds linking research and forecasting operations. *Bull. Amer. Meteor. Soc.,* **94,** 1187–1211, doi:10.1175/BAMS-D-12-00080.1.

——, T. Coleman, P. J. Neiman, R. J. Zamora, and M. D. Dettinger, 2013b: Observed impacts of duration and seasonality of atmospheric-river landfalls on soil moisture and runoff in coastal Northern California. *J. Hydrometeor.,* **14,** 443–459, doi:10.1175/JHM-D-12-076.1.

Rodhe, H., and J. A. N. Grandell, 1972: On the removal time of aerosol particles from the atmosphere by precipitation scavenging. *Tellus,* **24A,** 442–454, doi:10.1111/j.2153-3490.1972.tb01571.x.

Rosenfeld, D., Y. Rudich, and R. Lahav, 2001: Desert dust suppressing precipitation: A possible desertification feedback loop. *Proc. Natl. Acad. Sci. USA,* **98,** 5975–5980, doi:10.1073/pnas.101122798.

Steiner, M., O. Bousquet, R. A. Houze Jr., B. F. Smull, and M. Mancini, 2003: Airflow within major Alpine river valleys under heavy rainfall. *Quart. J. Roy. Meteor. Soc.,* **129,** 411–431, doi:10.1256/qj.02.08.

Weber, B. L., D. B. Wuertz, D. C. Welsh, and R. McPeek, 1993: Quality controls for profiler measurements of winds and RASS temperatures. *J. Atmos. Oceanic Technol.,* **10,** 452–464, doi:10.1175/1520-0426(1993)010<0452:QCFPMO>2.0.CO;2.

White, A. B., J. R. Jordan, B. E. Martner, F. M. Ralph, and B. W. Bartram, 2000: Extending the dynamic range of an S-band radar for cloud and precipitation studies. *J. Atmos. Oceanic Technol.,* **17,** 1226–1234, doi:10.1175/1520-0426(2000)017<1226:ETDROA>2.0.CO;2.

——, D. J. Gottas, E. Strem, F. M. Ralph, and P. J. Neiman, 2002: An automated brightband height detection algorithm for use with Doppler radar spectral moments. *J. Atmos. Oceanic Technol.,* **19,** 687–697, doi:10.1175/1520-0426(2002)019<0687:AABHDA>2.0.CO;2.

——, P. J. Neiman, F. M. Ralph, D. E. Kingsmill, and P. O. G. Persson, 2003: Coastal orographic rainfall processes observed by radar during the California Land-Falling Jets Experiment. *J. Hydrometeor.,* **4,** 264–282, doi:10.1175/1525-7541(2003)4<264:CORPOB>2.0.CO;2.

——, and Coauthors, 2013: A twenty-first-century California observing network for monitoring extreme weather events. *J. Atmos. Oceanic Technol.,* **30,** 1585–1603, doi:10.1175/JTECH-D-12-00217.1.

Yin, Y., Z. Levin, T. G. Reisin, and S. Tzivion, 2000: The effects of giant cloud condensation nuclei on the development of precipitation in convective clouds—A numerical study. *Atmos. Res.,* **53,** 91–116, doi:10.1016/S0169-8095(99)00046-0.

Zhang, J., and Y. Qi, 2010: A real-time algorithm for the correction of brightband effects in radar-derived QPE. *J. Hydrometeor.,* **11,** 1157–1171, doi:10.1175/2010JHM1201.1.